Mineralium Deposita (2025) 60:1643–1662
https://doi.org/10.1007/s00126-025-01363-x

ARTICLE

The magmatic-hydrothermal transition recorded by trace elements in quartz: a case study from the Zaaiplaats Tin Field, South Africa

L. C. Vonopartis[1,2] · P. A. M. Nex[1] · J. A. Kinnaird[1] · L. J. Robb[1,3] · R. Bolhar[1]

Received: 24 July 2024 / Accepted: 22 March 2025 / Published online: 9 April 2025

Abstract

The composition of quartz has historically been considered unimportant for mineral exploration, although this perspective is changing with the advancement of analytical techniques. The ability to measure trace element variations in quartz provides a unique window into the evolution of mineral deposits. Granites are currently of interest as they can host late-stage magmatic-hydrothermal mineralisation, such as Sn and other critical metals. The Nebo, Bobbejaankop, and Lease granites in the Zaaiplaats Tin Field of the Bushveld Complex represent well-exposed expressions of endogranitic Sn-mineralisation. These granites display an upward increase in their degree of hydrothermal alteration. Disseminated Sn-mineralisation is restricted to the Bobbejaankop and Lease granites and high-grade cassiterite-bearing tourmaline-quartz hydrothermal pipes that radiate upwards through these granites, terminating below the roof contact. Trace element compositions of the quartz from the Zaaiplaats Tin Field shows evidence that supports the suggested fractionation and fluid-saturation models of ore genesis. The Al/Ti and Ge/Ti ratios in quartz increase from the base to the roof and illustrate the sequential fractionation and increase in the degree of fluid-rock interaction. The trace element data display a shift from a magmatic fractionation-controlled evolution to a hydrothermally-controlled system influenced by the saturation of a late-stage magmatic-hydrothermal fluid. Thus, trace element variations in quartz can record the point of fluid-saturation and the magmatic-hydrothermal transition. Therefore, the recognition of the most evolved, fluid-saturated facies indicates lithologies with the best mineralisation potential for cassiterite. The use of trace elements in quartz extends beyond granite-hosted deposits and is potentially applicable to various mineralised systems.

Keywords Bushveld Complex · Granites · Magmatic-hydrothermal transition · Quartz · Tin · Trace elements in quartz

Introduction

Quartz is a ubiquitous mineral in the Earth's crust, yet research into its trace element variation is a relatively recent endeavour (Breiter et al. 2020; Götze et al. 2021; Müller et al. 2021). Quartz is stable across a large physiochemical range, and despite being compositionally simple (>99 wt% SiO_2), it exhibits appreciable crystallographic structural complexities and elemental substitution that reflects the environment of crystallisation (Fig. 1) (Howie et al. 1992; Götze et al. 2004, 2021; Götze 2009; Heaney et al. 2018). Thus, trace elements in quartz have been used to help characterise various plutonic, volcanic, metamorphic, pegmatitic, and hydrothermal lithologies – this has been comprehensively summarised by Breiter et al. (2020).

Crystallographic anomalies in quartz include point defects, dislocations, twinning, and three-dimensional defects that are related to thermodynamic conditions during crystallisation (Howie et al. 1992; Götze et al. 2004, 2021; Götze 2009; Heaney et al. 2018). Variations in the trace element content of quartz have been applied to the understanding and interpretation of the evolution and mineralisation of many ore deposits (Suttner and Leininger 1972; Hallbauer 1992; Monecke et al. 1999, 2002; Müller et al. 2003, 2008,

Editorial handling: B. Lehmann

✉ L. C. Vonopartis
Leonidas.Vonopartis@wits.ac.za

[1] School of Geosciences, University of the Witwatersrand, Private Bag 3, Johannesburg 2000, South Africa

[2] African Research Centre for Ore System Science, School of Geosciences, University of the Witwatersrand, 1 Jan Smuts Ave, Johannesburg 2000, South Africa

[3] Department of Earth Sciences, University of Oxford, Oxford OX1 3AN, UK

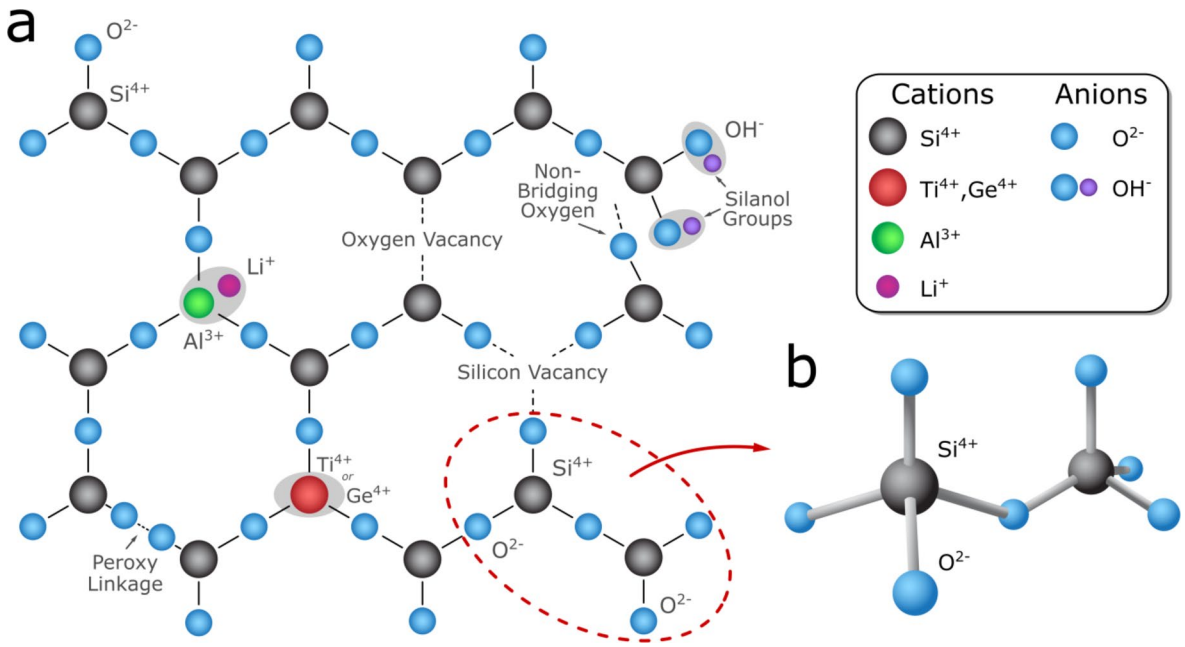

Fig. 1 Schematic representations of the crystallographic structure of quartz. (**a**) Plan view of a β-quartz lattice with common types of defects, after Götze (2009). (**b**) Structure of $[SiO_4]^{4-}$ tetrahedra joined by a common O^{2-} atom (Nesse 2009; Heaney et al. 2018)

2021; Larsen et al. 2004, 2009; Götze 2009; Jacamon and Larsen 2009; Uysal et al. 2011; Cui et al. 2019; Hong et al. 2019; Keyser et al. 2023). However, there has been no work on the quartz compositions from the mineralisation associated with the granites of the Bushveld Complex.

The Bushveld Complex is the largest igneous province on Earth with an approximate area of 90,000 km^2 and a volume of 450,000 km^3 (Fig. 2a) (Finn et al. 2015; Zeh et al. 2015; Scoates et al. 2021). The Bushveld Complex intruded the Transvaal Supergroup at 2.05 Ga (Zeh et al. 2015; Scoates et al. 2021) in the centre of the Kaapvaal Craton and is exposed in three major limbs that are connected at depth (Webb et al. 2011). The Bushveld Complex comprises a sill-like, mafic Rustenburg Layered Suite that was emplaced beneath the simultaneous extrusion of the Rooiberg Group volcanics (Robb et al. 2000; Zeh et al. 2015; Skursch et al. 2020). The Lebowa Granite Suite intruded through the Rustenburg Layered Suite to form the largest A-Type granite body on Earth. The Lebowa Granite Suite is enclosed between the mafic Rustenburg Layered Suite (below) and the felsic volcanics of the Rooiberg Group, as well as the Rashoop Granophyre Suite (above) (Robb et al. 2000; Bailie and Robb 2004; Skursch et al. 2020).

The Lebowa Granite Suite, also informally known as the "Bushveld Granites", is subdivided into several phases with the most prominent being the coarse-grained Nebo Granite (SACS 1980; Robb et al. 2000; Kinnaird et al. 2004). Unlike the mafic Rustenburg Layered Suite, the Lebowa Granite Suite does not host numerous world-class mineral deposits. However, it does host notable fluorite and polymetallic magmatic-hydrothermal endo- and exogranitic deposits and forms part of the so-called South African tin province (Wilson and Anhaeusser 1998; Robb et al. 2000; Crocker et al. 2001).

The Zaaiplaats Tin Field (ZTF) in the Northern Limb of the Bushveld Complex is a good example of endogranitic tin mineralisation. The granites that comprise the ZTF include the unmineralised Nebo Granite and the partially mineralised Bobbejaankop and Lease granites (Fig. 2c). Mineralisation in the tin field is found as low-grade disseminated cassiterite and within high-grade greisenised hydrothermal pipes and lenticular ore bodies (Strauss 1954; Crocker et al. 2001; Vonopartis et al. 2021). These granites provide a unique opportunity to use trace elements in quartz to investigate the mineralisation of an endogranitic Sn-mineralised system.

Trace element analyses of quartz, using laser ablation sector-field inductively-coupled plasma mass spectrometry (LA-SF-ICP-MS), were undertaken from the various lithologies in the ZTF (Supplementary Table 1). This research provides the first set of quartz trace element data from the Bushveld Complex and describes the magmatic-hydrothermal transition and potential use of trace elements in quartz to vector late-stage granitic hydrothermal mineralisation.

Zaaiplaats Tin Field

The historic Zaaiplaats and Groenfontein tin mines are part of the ZTF, which in turn forms part of the Lebowa Granite Suite along the Northern Limb of the Bushveld Complex

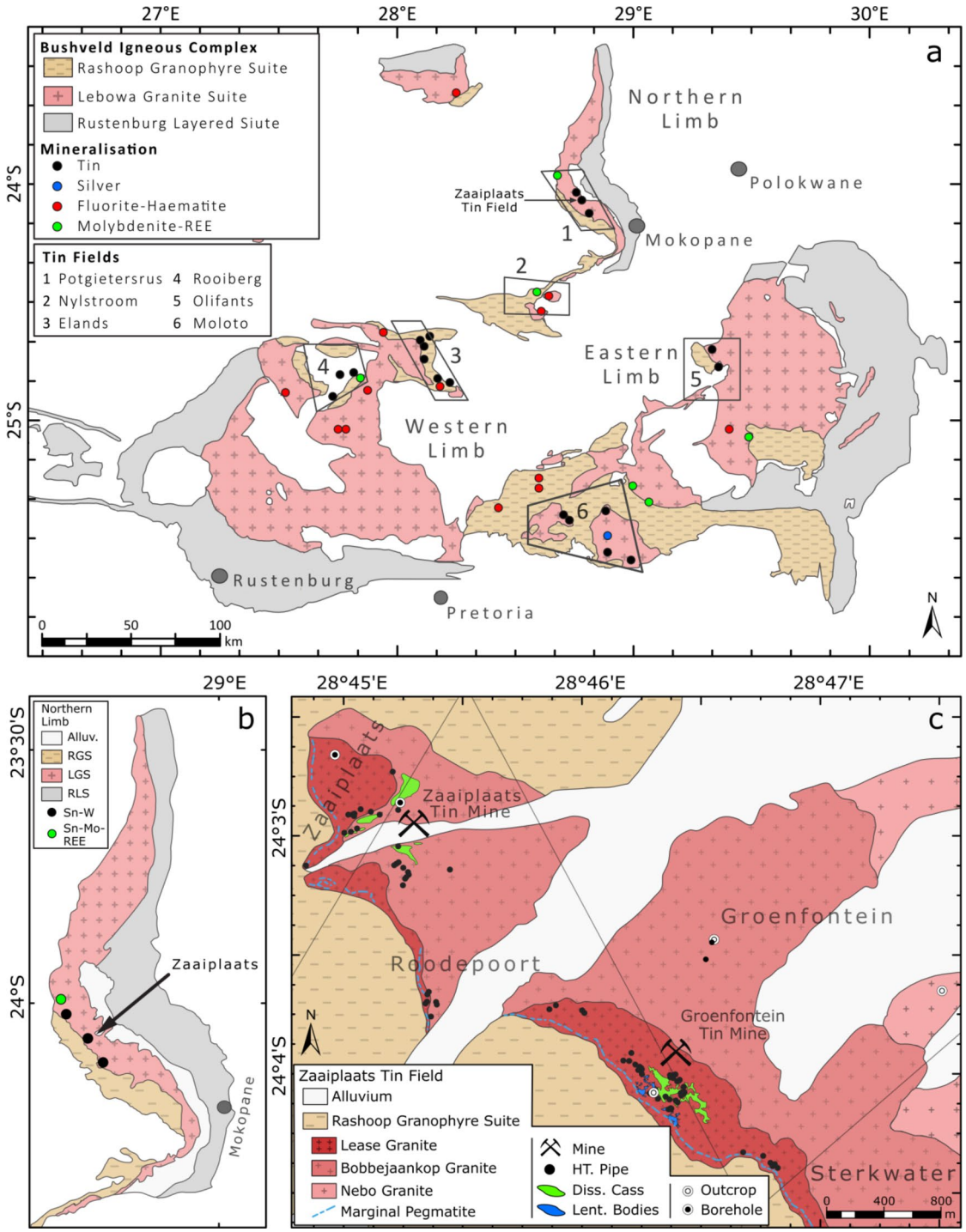

Fig. 2 Geological map of the (**a**) Bushveld Complex. Localities of tin, silver, fluorite-haematite, and molybdenite-REE mineralisation are displayed by coloured circles. Numbered blocks represent different tin fields. (**b**) Northern Limb of the Bushveld Complex and (**c**) Zaaiplaats Tin Field. Locations of outcrop sample sites and collars of the sampled borehole core shown by white circles (Supplementary Table 1). Abbreviations: Alluvium (Alluv.); Rashoop Granophyre Suite (RGS); Lebowa Granite Suite (LGS); Rustenburg Layered Suite (RLS); Hydrothermal Pipe (HT. Pipe); Disseminated Cassiterite (Diss. Cass.); and Lenticular Bodies (Lent. Bodies). Maps modified after Hunter (1975), Coetzee (1984), Wilson and Anhaeusser (1998), Crocker et al. (2001), and Vonopartis et al. (2021)

(Fig. 2). The ZTF is comprised of a sequence of granites, with the Nebo Granite at the base grading into the Bobbejaankop Granite, which has a sharp contact with the Lease Granite in the roof of the complex. This sequence of granites is capped by a red granophyre that forms part of the Rashoop Granophyre Suite (Fig. 2) (Strauss 1954; SACS

1980; Vonopartis et al. 2020). The Nebo Granite is an extensive granitic body, and in the ZTF it is expressed as an equigranular grey coarse-grained hornblende-bearing granite that grades upwards into a reddened coarse-grained biotite granite as it approaches the Bobbejaankop Granite (Strauss 1954; Hill et al. 1996; Kinnaird et al. 2004). The overlying Bobbejaankop Granite is shown to be the result of fractionation and pervasive hydrothermal alteration of the Nebo Granite (Strauss 1954; Kinnaird et al. 2004; Vonopartis et al. 2020). The Bobbejaankop Granite exhibits a characteristic brick-red coarse-grained texture, composed of reddened alkali-feldspar with discrete synneusis-textured quartz, and chloritised interstitial biotite. Miarolitic cavities, filled with euhedral quartz, red alkali-feldspars, fluorite, cassiterite, and tourmaline, are disseminated throughout the Bobbejaankop Granite and range from centimetres to metres in scale (Pollard et al. 1991; Kinnaird et al. 2004; Vonopartis et al. 2020).

The Lease Granite is a fine-grained red granite that forms the cupola of the Bobbejaankop Granite and is considered the product of late-stage magmatic-hydrothermal fluid saturation in the roof of the Bobbejaankop Granite (Strauss 1954; Coetzee 1984; Crocker et al. 2001; Vonopartis et al. 2020). The Lease Granite is composed of quartz with red alkali-feldspar and interstitial micas that show variable degrees of epidotisation, extensive chloritisation, and subsequent sericitisation (Strauss 1954; Pollard et al. 1991; Kinnaird et al. 2004; Vonopartis et al. 2020). Different styles of cassiterite mineralisation are present in the ZTF, including low-grade disseminations within zones of the Bobbejaankop Granite roof and centre of the Lease Granite, high-grade concentrations in large diameter greisenised lenticular ore bodies, and high-grade cassiterite-bearing sericite-tourmaline pipes that radiate from the centre of the Bobbejaankop Granite towards the roof of the Lease Granite (Coetzee 1984; Pollard et al. 1989; Crocker et al. 2001; Vonopartis et al. 2020).

Methodology

Cathodoluminescence and scanning electron microscopy

Cathodoluminescence (CL) and backscattered electron (BSE) images were obtained on thick-sections (300 µm) using a CAMECA SX5-FE electron probe micro-analyser at the University of the Witwatersrand. These CL images revealed various textures that are indicative of magmatic and hydrothermal growth during the crystallisation of the quartz (Rusk and Reed 2002). The CL and BSE images were used to map quartz grains prior to trace element analyses, to identify different quartz generations, and avoid defects and inclusions where possible.

Laser ablation inductively coupled plasma mass spectrometry

A total of 161 laser ablations were undertaken on quartz grains from the Nebo Granite, Bobbejaankop Granite, Lease Granite, and hydrothermal pipe from the ZTF. The thick-sections were polished to a surface with less than 1 to 2 µm variation and were analysed using the LA-SF-ICP-MS system in the Mass Spectrometry Facility at the University of the Witwatersrand. Trace elements in quartz were analysed employing an Applied Spectra/Australian Scientific Instruments (ASI) Resolution 193 nm ArF excimer laser coupled to a Thermo Fisher Scientific sector field inductively coupled plasma mass spectrometer (Element XR). Measurements were performed in low resolution and electrostatic scanning (E-scan) modes. The data were acquired by single spot analysis (64 µm diameter) using a laser repetition rate of 10 Hz and a fluence of 3.5 J/cm^2. The total signal acquisition time was 50 s, separated into 10 s of pre- and post-ablation (gas blank) and 30 s of ablation measurements. Laser sampling took place in a SE155 dual-volume ablation cell (Laurin Technic, Canberra, Australia) using a mixed He-Ar atmosphere with minor N_2 for enhanced signal stability and sensitivity (Hu et al. 2008). The gas flow conditions were: He (350 ml/min); Ar (1000 ml/min); N_2 (5 ml/min). Synthetic glass NIST-612 (Jochum et al. 2011) served as the primary calibration standard, with synthetic glass NIST-614 (Gao et al. 2002) and one natural quartz (Audétat et al. 2015) as secondary standards to ensure accuracy and precision. Line scans using NIST-612 glass were used to tune maximum sensitivity for ^{59}Co, ^{115}In, and ^{232}Th, while maintaining thorium oxide levels (ThO^+/Th) below 0.2%. The isotope ^{29}Si (99.95 wt% SiO_2) was used for internal standardisation. Two analyses of the primary calibration standard were obtained at the beginning and end of an experiment. There were between ten and twenty analyses of unknowns followed by the analyses of one primary and each secondary standard as quality control. Two laser pulses were used before each spot analysis to ensure a clean ablation surface. The following isotopes were measured: ^{7}Li, ^{9}Be, ^{11}B, ^{23}Na, ^{27}Al, ^{29}Si, ^{39}K, ^{44}Ca, ^{49}Ti, ^{55}Mn, ^{57}Fe, ^{72}Ge, ^{85}Rb, ^{88}Sr, ^{118}Sn, ^{137}Ba, ^{182}W, ^{232}Th, and ^{238}U. Depending on signal intensity, isotopes were measured in triple mode (pulse counting, analogue, and Faraday cup). Many of the elements did not prove informative, thus only a subset is presented and discussed. The complete set of quartz analyses are provided in Supplementary Table 2.

The trace element data reduction was accomplished using the iolite extension (http://www.iolite.org.au) of the softwar

e Igor Pro (http://www.wavemetrics.com). Specifically, the data reduction scheme "X_Trace_Elements_IS", was run in a series of sequential steps, including data import, selection of integrations, baseline subtraction, drift and down-hole fractionation, calibration, and error propagation (Paton et al. 2010, 2011). Due to a lack of coexisting rutile, Ti-in-quartz geothermometry was not attempted. References to temperature are made strictly based on the correlation that Ti abundance decreases in quartz with a decrease in the temperature of crystallisation (Wark and Watson 2006; Huang and Audétat 2012). Therefore, the interpretations regarding temperature are not based on geothermometers.

Results

Cathodoluminescence textures of quartz

Cathodoluminescence images of quartz from the granites and hydrothermal pipe revealed various generations, textures, and zonations. These images were used to guide the LA-SF-ICP-MS analysis and describe the textural variations and generations of quartz. The generations of quartz are denoted alphabetically, beginning at the crystal core (e.g. Qz-A), and labelled towards the rim of the quartz crystal (e.g. Qz-B, Qz-C, etc.). Detailed petrographical descriptions of these lithologies were reported by Vonopartis et al. (2020).

Nebo granite quartz

The Nebo Granite is the stratigraphically lowest granite in the ZTF. The Nebo quartz is subrounded, magmatic, coarse-grained (400 to 2,000 µm), and crystallised amongst subhedral alkali-feldspars and interstitial biotite (Fig. 3). The CL imaging shows little to no zonation (Fig. 3a, b), although the quartz occasionally exhibits a strongly luminescent core surrounded by a less luminescent quartz rim (Fig. 3c-f).

There are at least two generations of quartz described in the Nebo Granite as shown by CL, an early strongly luminescent core (Qz-A) and a later slightly weaker luminescent rim (Qz-B) (Fig. 3c, d). The Qz-B rims are typically < 200 µm thick and define the boundary between the quartz grain and other minerals (Fig. 3d). There is a concentric growth outward from a euhedral Qz-A core, without any visible zonation and minor growth impingements, caused by the obstructive growth of an adjacent mineral (Fig. 3f). The cores of the quartz crystals occasionally display very fine (< 10 µm) concentric oscillatory zonation attributed to self-organisation during crystallisation (Fig. 3d) (Müller et al. 2000). Both generations of quartz are inclusion-poor, although there are many small (< 5 µm) luminescent phases along fractures. Some fractures are healed by a non-luminescent quartz generation (Qz-C) (Fig. 3b, f).

Bobbejaankop granite quartz

The medium- to coarse-grained quartz crystals (200 to 2,600 µm) from the Bobbejaankop Granite are generally zoned in CL images. However, the largest quartz grains do not show compositional zonation but do exhibit extensive oscillatory growth (Fig. 4a). Most of the quartz in the Bobbejaankop Granite typically hosts a strongly luminescent (Qz-A) sub- to euhedral core with a 100 to 200 µm thick weakly luminescent (Qz-B) rim in CL (Fig. 4b, c). Both the Qz-A and Qz-B generations exhibit very fine (< 10 µm) oscillatory zonation that developed parallel to the internal generational boundaries. The interior Qz-A variety has sharp edges that meet at coigns, which are somewhat rounded more often than sharp (Fig. 4b). The Qz-B rims of these grains are considerably more irregular and define the final growth stage of the crystal (Fig. 4b-d).

The quartz does not host many large mineral inclusions, although both generations are cross-cut by fractures that are annealed by a non-luminescent variety of quartz (Qz-C). Many small (100 to 900 µm) subrounded quartz crystals that resemble the Qz-B generation and smaller (< 10 µm) anhedral Qz-C grains are disseminated interstitially within the finer-grained groundmass. Many adjacent quartz crystals are commonly connected/welded by the non-luminescent Qz-C generation resulting in the characteristic synneusis texture of quartz in the Bobbejaankop Granite (Fig. 4e, f) (Vonopartis et al. 2020; Dyck 2023).

The quartz within miarolitic cavities lacks oscillatory zonation, although it exhibits distinct compositional zonation (Fig. 4g, h). Crystals range from 500 to 1,000 µm in diameter and occasionally exhibit double terminations. The crystals have weakly luminescent cores that resemble the Qz-B generation in the main granitic assemblage (Fig. 4g). These Qz-B cores are surrounded by thin (5 to 10 µm) rims of Qz-C (Fig. 4g). Of note is that quartz crystals within the miarolitic cavities are adjacent to strongly altered mica and feldspar, and are usually outlined by a thin (5 to 10 µm) strongly luminescent rim (Fig. 4h).

Lease granite quartz

The quartz from the Lease Granite is notably variable when viewed under CL. These crystals are sub- to euhedral and have the smallest grain size (100 to 1,500 µm) (Fig. 5). The largest crystals contain two to three quartz generations, with a non-luminescent quartz phase infilling the healed fractures (Fig. 5a, b). In CL, the large crystals exhibit a moderately luminescent euhedral core (Qz-A) surrounded by a 100 to

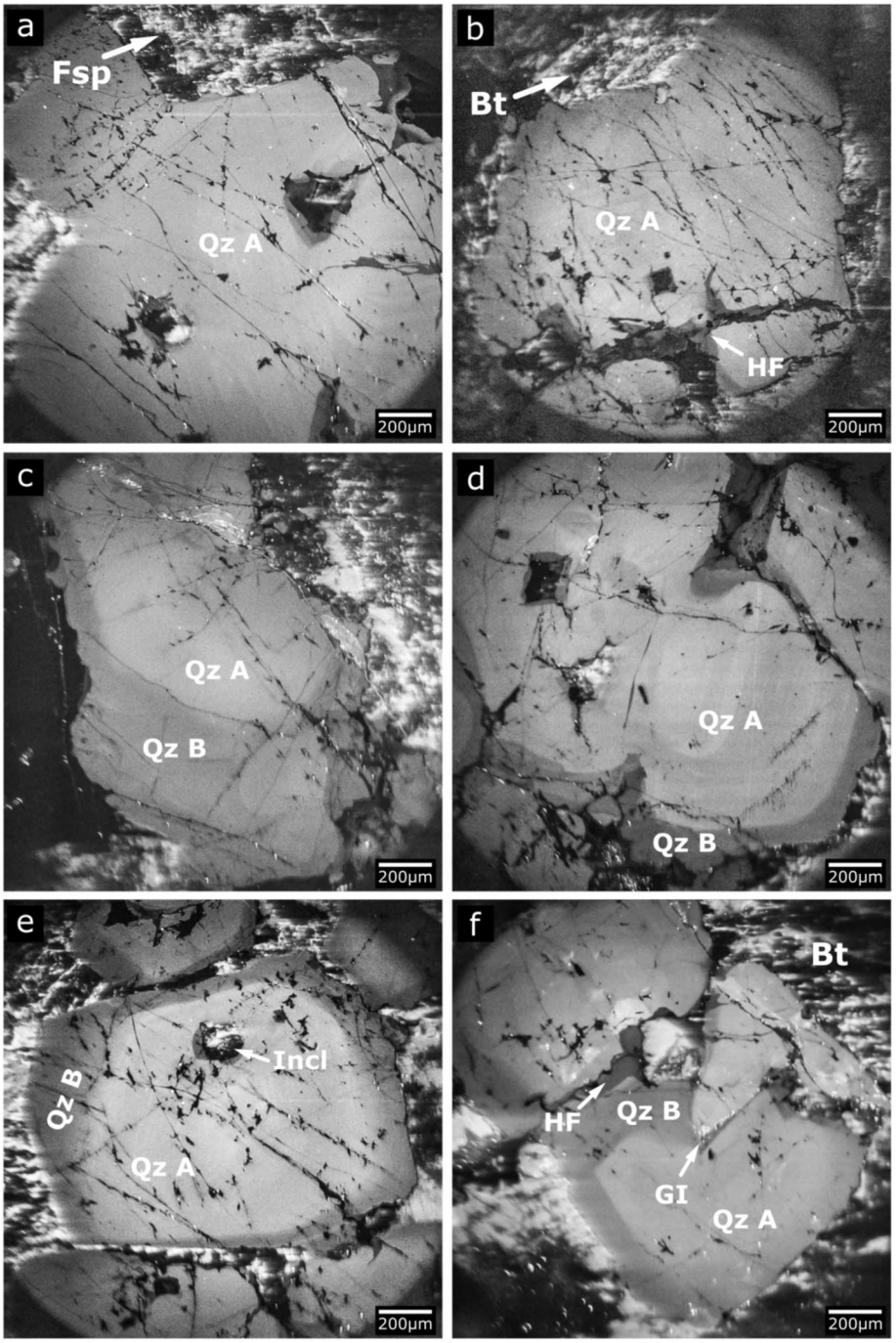

Fig. 3 CL images of quartz from the Nebo Granite. (**a**) An unzoned quartz of Qz-A generation. (**b**) A Qz-A grain with healed fractures. (**c**) A slightly zoned quartz with a Qz-A core and a darker Qz-B rim. (**d**) A zoned quartz with an oscillatory zoned Qz-A core, and a darker Qz-B rim. (**e**) A zoned quartz with a Qz-A core hosting a large mineral inclusion, and darker Qz-B rim. (**f**) A subhedral zoned quartz with a Qz-A core and a darker Qz-B rim with a growth impingement. Abbreviations: Quartz (Qz); healed fractures (HF); growth impingement (GI); inclusion (Incl); feldspar (Fsp); and biotite (Bt)

200 µm thick, slightly more luminescent (Qz-B) zone. This second generation is enclosed by a 100 to 300 µm thick rim of a weakly luminescent quartz (Qz-C) phase (Fig. 5a-d). Oscillatory zonation is common in all quartz generations with growth impingements caused by neighbouring minerals, and possibly the adhesion of fluid-rich melt droplets on the crystal surface (Fig. 5d) (Müller et al. 2000).

The growth and shape of the oscillatory and compositional zonations of the Qz-A and -B generations maintain the euhedral nature of the quartz crystal. The marginal Qz-C generation terminates with an irregular nature and results in an overall subrounded grain (Fig. 5c, d). Most of the quartz grains are medium- to fine-grained (< 1,000 µm) and lack a bright Qz-A core. They comprise a euhedral Qz-B core and subhedral to subrounded 100 to 300 µm Qz-C rim (Fig. 5d). Healed fractures are infilled by a later non-luminescent quartz generation (Qz-D). Large mineral inclusions are uncommon in the Lease quartz, although they contain many luminescent phases.

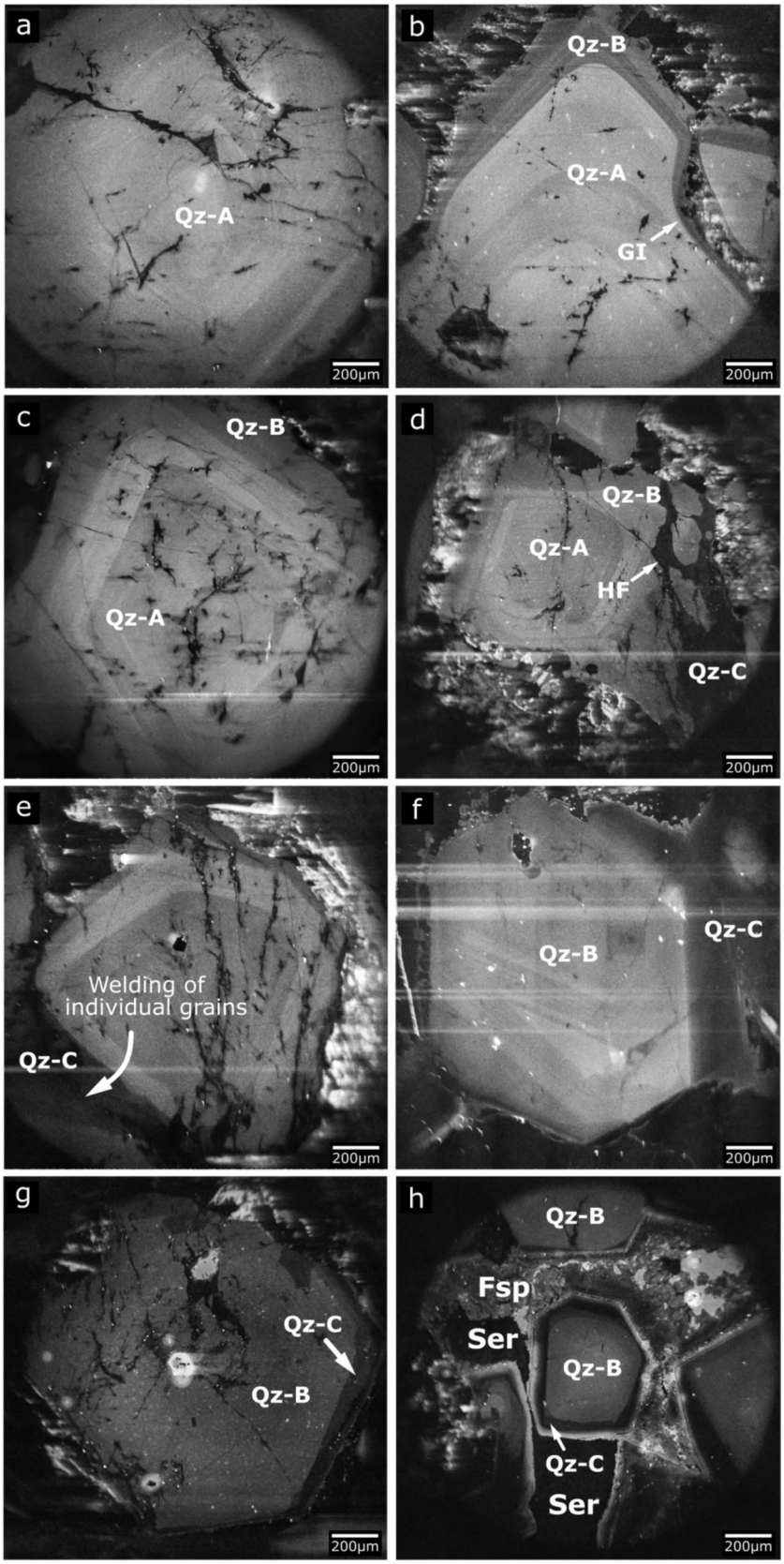

Fig. 4 CL images of quartz from the Bobbejaankop Granite. (**a**) A large oscillatory zoned Qz-A crystal. (**b**) A coarse-grained subhedral quartz with an oscillatory zoned Qz-A core with a darker Qz-B rim and a notable growth impingement. (**c**) A large fractured subhedral quartz with a well-developed oscillatory zoned Qz-A core, surrounded by a darker Qz-B rim. (**d**) A medium-grained fractured quartz crystal exhibiting an oscillatory zoned Qz-A core, surrounded by a darker Qz-B rim. Healed fractures are infilled by the Qz-C generation. (**e**) A subhedral quartz grain with well-developed oscillatory and compositional zonation. Quartz crystals are welded to adjacent quartz crystals by the Qz-C generation. (**f**) A subhedral oscillatory zoned Qz-B quartz welded to an adjacent grain by a Qz-C generation. (**g**) A large Qz-B crystal with a thin Qz-C rim. (**h**) A small crystal with a Qz-B core surrounded by Qz-C and a bright quartz rim. Abbreviations: Quartz (Qz); feldspar (Fsp); healed fractures (HF); sericite (Ser); and growth impingement (GI)

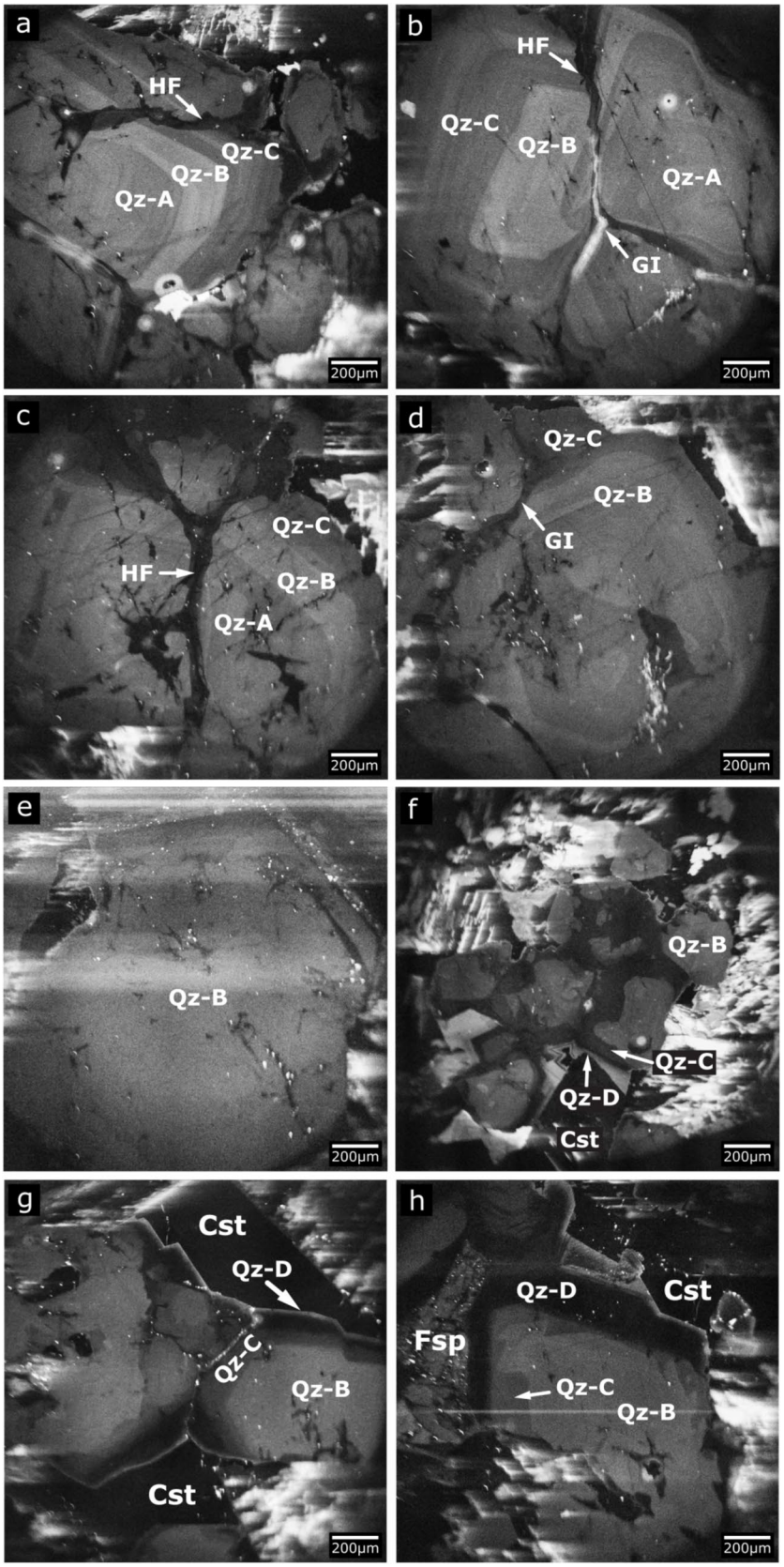

Fig. 5 CL images of quartz from the Lease Granite. (**a**) A fractured coarse-grained quartz crystal, exhibiting well-developed oscillatory zonation in a Qz-A core surrounded by a Qz-B zone then a Qz-C rim and healed fractures. (**b**) A large, fractured quartz with a core of Qz-A core then a Qz-B zone and a rim of Qz-C, with a growth impingement. (**c**) A large quartz with clear oscillatory and compositional zonation with a Qz-B core, Qz-C rim, and infilled healed fractures. (**d**) A quartz with oscillatory zoned Qz-B core, Qz-C rim, and growth impingements. (**e**) A homogeneous euhedral Qz-B quartz crystal. (**f**) Small chained Qz-B quartz linked by a Qz-C generation and intergrown with euhedral cassiterite. (**g**) Euhedral Qz-B quartz crystals are surrounded by a Qz-C zone, then a Qz-D zone with a thin ring of brightly luminescent quartz, proximal to euhedral cassiterite. (**h**) A large Qz-B crystal with Q-C sectors and a Qz-D rim, lined by a bright quartz ring, adjacent to cassiterite. Abbreviations: Quartz (Qz); feldspar (Fsp); cassiterite (Cst); healed fractures (HF); and growth impingement (GI)

The quartz crystals within miarolitic cavities are smaller (< 600 µm) and sub- to euhedral. The miarolitic quartz lacks large compositional zonation in CL and is either solely composed of Qz-B or Qz-C, or have a Qz-B core and a Qz-C rim (Fig. 5e-h). These miarolitic quartz crystals terminate as euhedral grains and are commonly welded to two or three neighbouring euhedral crystals by the non-luminescent Qz-D generation (Fig. 5f-h). The Qz-D generation is restricted to healed fractures in the main granitic assemblage, although it is a notable component within miarolitic quartz. Some of these miarolitic quartz crystals exhibit a euhedral Qz-B core, surrounded by a Qz-C overgrowth and then a non-luminescent Qz-D generation. Like the miarolitic quartz in the Bobbejaankop Granite, the non-luminescent Qz-D layer is outlined by a thin highly-luminescent rim proximal to strongly greisenised assemblages and adjacent to cassiterite crystals (Fig. 5f-h).

Tourmaline-quartz hydrothermal pipe quartz

The quartz in the hydrothermal pipes differs markedly from the quartz in the granitic lithologies. These crystals are set in a very fine-grained groundmass of radial tourmaline and are commonly trapped between the edges of acicular tourmaline fans. They are relatively pristine and inclusion-poor, although they contain highly luminescent phases along fractures and structural defects (Fig. 6). Some of the larger quartz crystals exhibit well-defined hexagonal structures that are indicative of β-quartz (Fig. 6a). Many euhedral quartz crystals have distinct sector zonation perpendicular to the c-axis (Fig. 6a-c). In CL, the euhedral hexagonal crystal cores are composed of strongly luminescent quartz (Qz-A) and lack oscillatory zonation. However, most of the quartz is medium-grained and exhibits well-defined trigonal (α-quartz) structures (Fig. 6b, c).

A later generation of quartz appears to have grown along the crystallographic faces of the euhedral cores (Fig. 6a-c). This later generation is differentiated into alternating luminescent Qz-A faces and less luminescent Qz-B faces. The individual sectors within the secondary generation exhibit very fine internal oscillatory zonation that developed parallel to the crystallographic faces of the euhedral core. Most of the crystal edges are well defined, although some display amorphous intergrowths with the tourmaline groundmass (Fig. 6). Some of the larger quartz crystals are heterogeneous under CL and display right-angled sector zonations when viewed parallel to the c-axis (Fig. 6d).

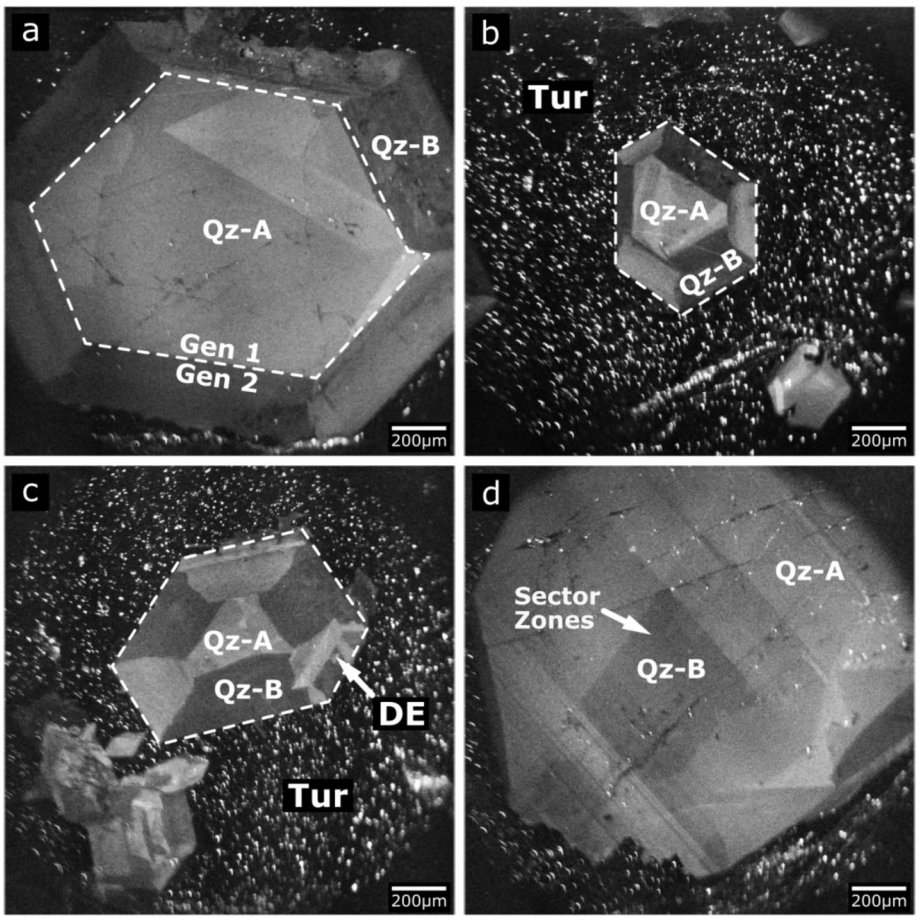

Fig. 6 CL images of quartz from a tourmaline-quartz hydrothermal pipe. (**a**) Large hexagonal (β-quartz) quartz crystal showing a bright Qz-A and darker Qz-B sector zonation. The quartz displays two generations: Generation 1 is an early hexagonal quartz core of Qz-A, and generation 2 is a rim of alternating Qz-A and Qz-B sectors. (**b**) Small trigonal (α-quartz) sector-zoned quartz set in a tourmaline matrix. (**c**) A trigonal sector-zoned quartz with a deformed edge, set in a tourmaline matrix. (**d**) The apex of a large quartz along the c-axis, displaying sector zonations of bright Qz-A and darker Qz-B. Abbreviations: Quartz (Qz); tourmaline (Tur); deformed edge (DE); and generation (Gen)

Trace elements in quartz

The most abundant trace element in the studied quartz is Al, which ranges from 41 to 930 ppm (Fig. 7). The Al content of the quartz increases sequentially through the Nebo, Bobbejaankop, and Lease granites and is highest in the hydrothermal pipe. Light elements such as Li exhibit a positive correlation with Al in quartz and generally increase from the Nebo and Bobbejaankop, which have comparable Li contents, to the Lease Granite and pipe quartz that are considerably more Li-enriched (Fig. 7a). The Li:Al atomic ratio of 1:1 defines an ideal charge compensation for Si^{4+} by Al^{3+} with the addition of Li^{+}. The magmatic quartz of the Nebo Granite plots close to the ideal Li:Al ratio, while the Bobbejaankop, Lease, and pipe quartz generally exhibit ratios greater than 1:2 (Fig. 7b). Data points above the ideal 1:1 line are common and attributed to analytical error and uncertainty (Müller et al. 2021).

The average B content increases from 1.5 ppm in the Nebo Granite quartz to 3.3 ppm in the Bobbejaankop quartz, 6.2 ppm in the Lease quartz, and 5.3 ppm in the pipe quartz (Fig. 7c). Quartz analyses with high concentrations of B in the Bobbejaankop and Lease granites may be attributed to the ablation of tourmaline micro-mineral inclusions (Müller et al. 2012; Götze et al. 2021) (Fig. 7c). Minor variations in the Na, K, and Ca contents of the quartz are generally < 1,000 ppm, although Ca in Lease quartz does exceed 1,000 ppm in several analyses (Fig. 7a). This feature can be attributed to the decrepitation of mineral/fluid inclusions, or the edges of underlying or adjacent minerals during ablation, such as calcite or fluorite. The Nebo quartz has the highest Ti and lowest Al content of the quartz populations. Despite slight variations there is notable Ti depletion and Al enrichment from the Nebo to Bobbejaankop and Lease quartz, along a "magmatic" quartz trend (Fig. 7d) (Müller et al. 2018; Hong et al. 2019), whereas some of the Bobbejaankop, Lease, and all the pipe quartz being distinctly Ti-poor.

Germanium is a common component in the cationic substitution of quartz and reflects a more hydrothermal environment (Götze et al. 2004; Jacamon and Larsen 2009; Breiter et al. 2014). The substitution of Ge in quartz is principally controlled by its presence in the crystallising environment and is enriched in late magmatic-hydrothermal fluids (Götze et al. 2004; Müller et al. 2018). At lower temperatures and under increasingly hydrothermal conditions, Ge^{4+} will be preferentially incorporated into quartz substituting for Si^{4+} (Fig. 1) (Götze et al. 2004; Larsen et al. 2004; Breiter et al. 2014). There is a systematic increase of Ge in quartz that correlates with an increase in Al from the Nebo, Bobbejaankop, and Lease granites, with the highest Ge content in the quartz from the hydrothermal pipe (Fig. 7e).

Other trace elements such as Rb, Sr, Zr, Hf, Sn, and W exhibit extreme variations because they are hosted within mineral and fluid inclusions (Götze 2009). Thus, they are not used in the interpretation of the system. However, it is noteworthy that the average Sn content of the quartz displays an increase, from the Nebo (0.17 ppm) to the Bobbejaankop (0.24 ppm), then to the Lease (1.49 ppm) granites, reflecting the increasing Sn in whole-rock compositions (Supplementary Fig. 1). Most analyses of the quartz from the hydrothermal pipe did not return detectable values of Sn, except for one that recorded 0.59 ppm (Fig. 7).

Quartz zonation

There were a total of sixty traverses, nine on quartz from the Nebo Granite, twenty-six on quartz from the Bobbejaankop Granite, twenty-two on Lease granite quartz, and three on pipe quartz to reveal trace element variations with respect to zonation (Supplementary Table 2). The core of the quartz grain is denoted "*point 1*" with the subsequent ablation sites sequentially numbered towards the rim (Fig. 8). Large visible defects and inclusions were avoided wherever possible, however, due to the diameter and depth of ablation this was not always possible. Therefore, the structurally incorporated elements Al, Ti, and Ge were compared to describe the evolution of the quartz crystals in this system. In addition, Sn was included to reveal any correlation with cassiterite mineralisation.

The quartz grains from the Nebo Granite are relatively homogeneous with Ti, Al, and Ge showing systematic behaviour suggesting direct cationic substitution. The Ti content decreases slightly from *point 1* (Qz-A) to *point 3* (Qz-B), while Al remains relatively constant (Fig. 8a; Table 1). The Sn content of the quartz in the Nebo Granite remains constant between 0.07 and 0.08 ppm (Fig. 8a). In the Bobbejaankop granite, the Al, Ti, and Ge contents of the quartz core (Qz-A) from *point 1* to *point 3* (Fig. 8b; Table 1), are similar to the Nebo quartz. The Ge content increases from below detection in the core of the Bobbejaankop quartz, to 1.02 and 1.05 ppm at points 3 and 4, respectively (Fig. 8b).

Tin in the Bobbejaankop quartz is below detection through points 1 to 3 and reaches 0.17 ppm at *point 4*. The Al and Ti content from points 1 to 3 of the Bobbejaankop quartz core (Qz-A) are similar to the magmatic Nebo quartz. At *point 4* the Al content in the rim of the Bobbejaankop quartz (Qtz-B) increases to 115 ppm and the Ti content decreases to 58 ppm. This compositional shift is accompanied by a marked decrease in the luminescence of the Bobbejaankop Qz-B generation (Fig. 8b). The quartz from the Bobbejaankop Granite can therefore be separated into two geochemically distinct generations: (1) A core of Qz-A (points 1 to 3) that has a greater Ti than Al content, is Ge-poor and has a high

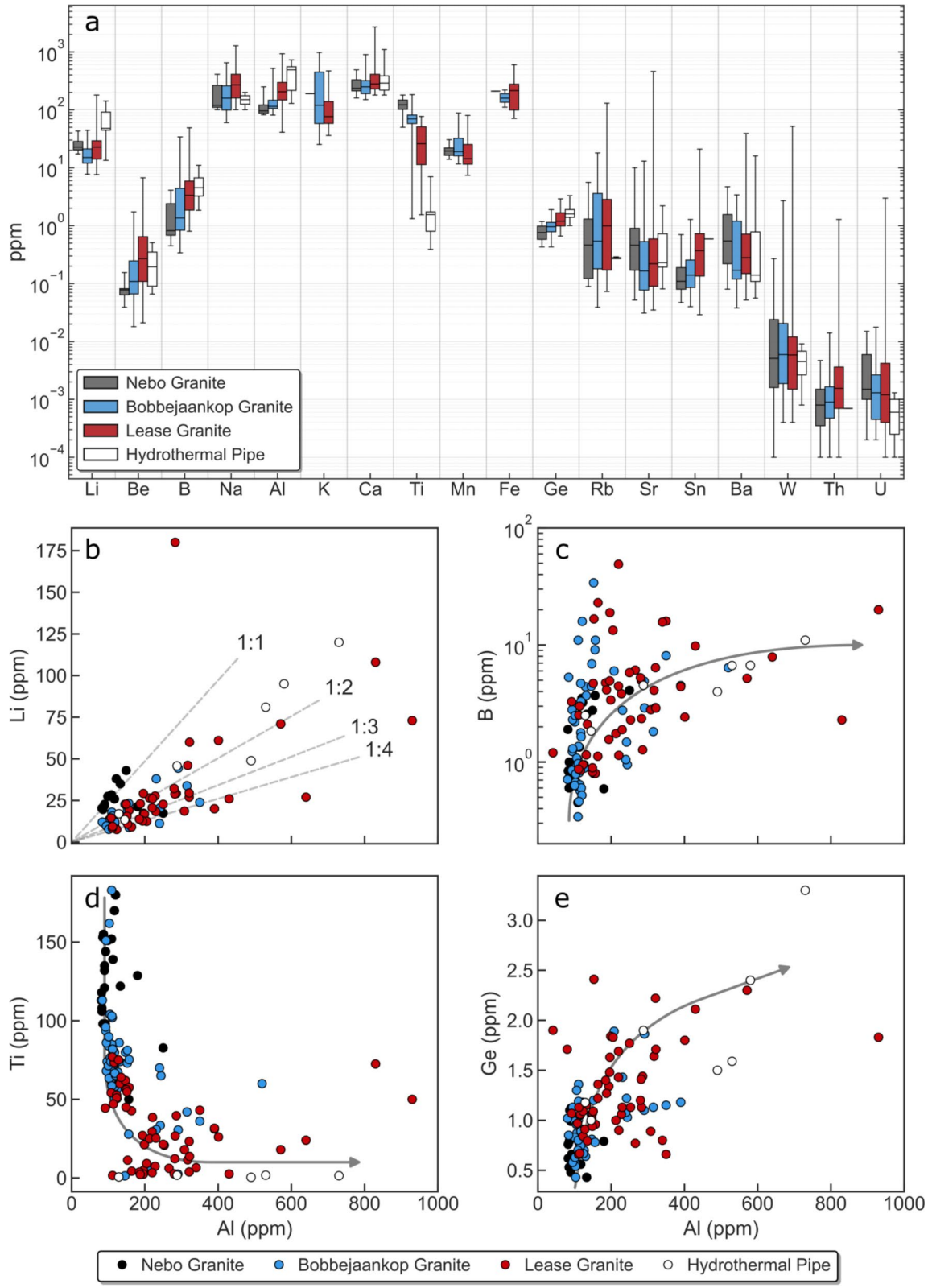

Fig. 7 Trace element compositions of quartz from the Zaaiplaats Tin Field. (**a**) Box and whisker diagram showing the trace element abundances. The median values are shown within each box as horizontal bar. Elements with values below detection limit are not shown. Graphs of selected trace elements plotted against Al. (**b**) Li vs. Al. Dashed lines indicate Li:Al ratios. The ratio of 1:3.89 corresponds with the ideal atomic Li:Al ratio of 1:1 (Müller et al. 2021). (**c**) B vs. Al. (**d**) Ti vs. Al. (**e**) Ge vs. Al. Grey arrows indicate the evolution of granitic system, from the least- to most-fractionated lithologies

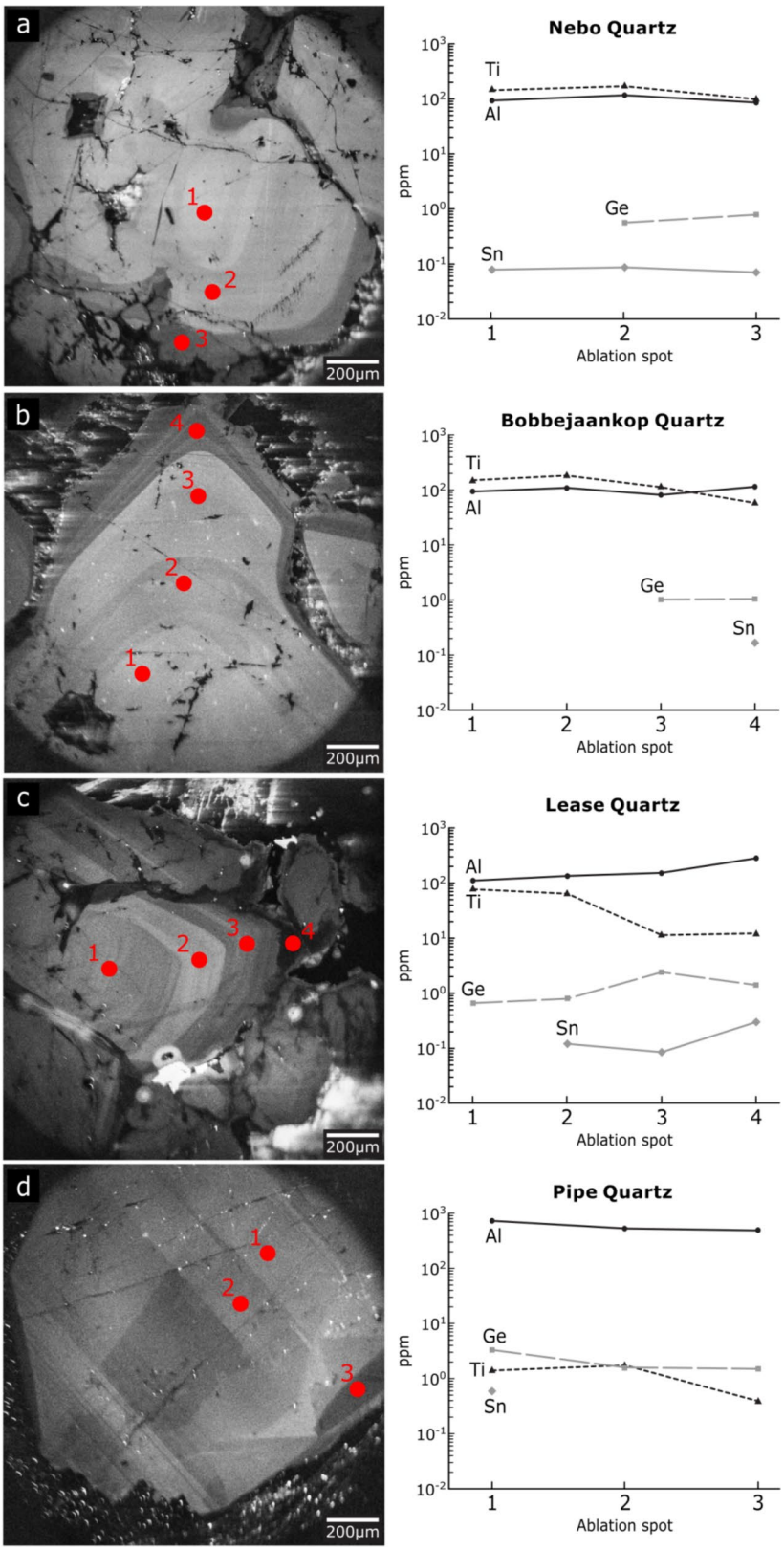

Fig. 8 Diagrams illustrating the ablation traverses across quartz crystals from the Zaaiplaats Tin Field. A CL image with ablation spots and corresponding trace element compositions of the quartz from the: (**a**) Nebo Granite, (**b**) Bobbejaankop Granite, (**c**) Lease Granite, and (**d**) Hydrothermal Pipe. Ablation spots are numbered sequentially from the core to the rim (red circles). Trace element values are provided in Table 1. Values below detection are not shown

Table 1 Trace element compositions for quartz analyses at each point along the traverses shown in Fig. 8. Values are provided in ppm

Lithology	Element	Point 1	Point 2	Point 3	Point 4
Nebo Granite	**Al**	93	117	86	
	Ti	144	170	98	
	Ge	-	0.56	0.79	
	Sn	0.08	0.08	0.07	
Bobbejaankop Granite	**Al**	94	109	81	115
	Ti	151	183	113	58
	Ge	-	-	1.02	1.05
	Sn	-	-	-	0.17
Lease Granite	**Al**	111	135	153	282
	Ti	77	64	11.3	12.2
	Ge	0.66	0.80	2.41	1.41
	Sn	-	0.12	0.09	0.30
Tourmaline-Quartz Pipes	**Al**	730	530	490	
	Ti	1.4	1.74	0.39	
	Ge	3.3	1.59	1.50	
	Sn	0.59	-	-	

Values below the detection limit are denoted with a "-"

CL luminescence signature; and (2) a rim of Qz-B (point 4) that has a greater Al than Ti content, and low CL luminescence and minor Ge and Sn.

The quartz from the Lease Granite differs from the earlier facies with a notable increase in Al and a decrease in Ti from core to rim (Fig. 8c; Table 1). The decrease in Ti is associated with a decreased luminescence and the variations in Ti show a slight inverse correlation with the Ge content of the Lease quartz (Fig. 8c). The Sn content in the Lease quartz is similar to the Nebo and Bobbejaankop quartz (Table 1). There is limited substitution of Sn into the silica tetrahedral site, even in cassiterite-bearing pegmatites and granites (Götze and Möckel 2012; Breiter et al. 2014, 2020; Müller et al. 2021). Therefore, any large variability in Sn content is likely related to micro-inclusions. The Lease quartz can be separated into two chemically distinct generations: (1) A core (points 1 and 2) of Qz-A and Qz-B with a moderate luminescence, that is similar to the later quartz generation of the Bobbejaankop Granite; and (2) a rim of low to non-luminescent Qz-C and -D (points 3 and 4), which displays an Al, Ge, and ± Sn enrichment and a Ti depletion relative to the core.

In the tourmaline pipes, although there is little chemical variation in the quartz, the composition of the quartz is markedly different from the quartz in the granites. The pipe quartz has the highest Al and Ge content and is markedly depleted in Ti compared to the quartz from the granitic lithologies (Fig. 8d; Table 1). The Al content of the large quartz crystal is homogeneous and does not show significant variations between the different sectors visible by CL (Fig. 8d). There is a decrease of both Ge and Ti, in particular, within the pipe quartz from points 1 to 3, whereas Ge and Ti are usually inversely related (Larsen et al. 2004; Jacamon and Larsen 2009; Breiter et al. 2014). There is a scarcity of measurable Sn in the pipe quartz, although the Sn content at *point 1* (0.59 ppm) is higher than in any other quartz (Fig. 8d).

Discussion

Contamination by fluid and mineral inclusions

The quartz crystals from the Zaaiplaats tin granites, particularly the Lease Granite, contain many inclusions. Due to the diameter of the beam and depth of the ablation process, some inclusions were unavoidably analysed.

Several measured trace elements, such as Na, Ca, Fe, Mn, Sr, U, Th, Sn, and W, are not present in all quartz analyses nor exhibit a significant correlation with Al, and therefore do not act as charge compensators during Al^{3+} substitution for Si^{4+} (Götze et al. 2004; Götze 2009). However, K and to a lesser extent Rb do display a slight correlation with Al. Thus, minor amounts of K and Rb likely acted as charge compensators for Al^{3+}, which may account for the deviation from the ideal Li:Al ratio in the quartz from the Bobbejaankop and Lease granites. Most of these trace elements may reflect contamination by trapped saline fluids and mineral inclusions (Götze 2009; Götze et al. 2021) and could be used to infer the composition of the magmatic to hydrothermal environment. However, these elements are considered to have large degrees of uncertainty, and any inferences based on these elements are made with caution.

Trace element substitution

Cations that readily substitute for Si^{4+} in the quartz tetrahedra, such as Al, Ti, Li, and Ge (Götze et al. 2004; Götze 2009; Müller and Koch-Müller 2009), are relatively abundant in quartz. The incorporation of Al into quartz is considered to increase with progressive fractionation of a melt (Müller et al. 2018). This substitution of Al^{3+} for Si^{4+} in the quartz tetrahedral site is charge balanced by the coupled cationic substitution of a monovalent cation, for example $Si^{4+} \leftrightarrow Al^{3+} + Li^{+}$ (Fig. 1) (Götze et al. 2004; Götze 2009; Müller et al. 2018). The positive correlation of Al and Li occurs in all lithologies at the ZTF. All phases of quartz in the Nebo granite follow the ideal Li:Al ratio of 1:1 (Fig. 7b), indicating that the majority of the Al^{3+} charge deficit is compensated by Li^{+}. In contrast, most of the quartz phases in the Bobbejaankop, Lease, and pipe quartz generally have an Li:Al ratio greater than 1:2. This may be due to the charge compensation being increasingly achieved with alternative trace elements, such as H^{+}, Na^{+}, or K^{+} (Müller et al. 2018), although Na and K do not show a strong correlation with Al.

Wark and Watson (2006) noted the correlation between Ti concentration and temperature in quartz, stating that $Ti^{4+} – Si^{4+}$ cationic substitution is more compatible during the early high-temperature magmatic stages of crystallisation. With decreasing temperature, Al becomes preferentially incorporated in lieu of Ti, increasing the Al/Ti ratio (Larsen et al. 2004; Wark and Watson 2006; Müller et al. 2010). The diadochy of Ti^{4+} for Si^{4+} in the quartz lattice provides insight into both the evolution and temperature of the crystallising quartz (Götze et al. 2004; Larsen et al. 2004; Müller and Koch-Müller 2009; Breiter et al. 2014). The higher-temperature "magmatic" quartz, in the Nebo granite and Bobbejaankop cores, have a higher Ti, lower Al, and are more CL luminescent than lower-temperature rim quartz of the Bobbejaankop granite and quartz cores in the Lease Granite. This steady decrease in Ti and increase in Al during fractionation, from the magmatic Nebo quartz, has resulted in notably low Ti and high Al content in the late hydrothermal pipe quartz.

The relationship between structurally incorporated cations in quartz can be demonstrated graphically using plots such as the Ti – Ge*10 – Al/10 (Ti-Ge-Al) ternary diagram (Schrön et al. 1988). This diagram was used by Breiter et al. (2014) to compare quartz from I-, S-, and A-Type granites and pegmatites (Fig. 9a). They showed that magmatic quartz evolved from Ti- to Al-rich compositions, while pegmatitic quartz evolved from a Ti- to more Ge-rich composition, with both of the quartz trends exhibiting a decrease in Ti from magmatic to hydrothermal quartz. The use of Al, Ti, and Ge and their ratios (Al/Ti and Ge/Ti) in quartz are useful proxies for the degree of progressive silicate melt fractionation (Larsen et al. 2004; Müller et al. 2010, 2018; Hong et al. 2019). The progressive fractionation of a granitoid corresponds to an increase in the Ge/Ti ratio of its quartz, as Ge increases in more hydrothermal conditions as previously described.

The Ti-Ge-Al ternary diagram shows that the quartz from the Zaaiplaats granites and hydrothermal pipe follows the compositional evolution of A-Type granitic quartz (Fig. 9a). The Nebo quartz clusters close to the Ti apex of the ternary diagram (magmatic quartz) and evolves with a decrease in Ti and a slight increase in Al and Ge content. The Bobbejaankop quartz compositions overlap with those of the quartz from the Nebo Granite (magmatic quartz), although the former exhibit a greater Ti-depletion and a marginally higher Al content. The Bobbejaankop quartz compositions evolve further along the A-Type granite fractionation trend, becoming significantly more "magmatic-hydrothermal" (Fig. 9a).

The Lease data is clustered at the lower Ti compositional end of the Bobbejaankop quartz compositional array, with a slightly higher Al content, within the magmatic sector of the ternary diagram (Fig. 9a). However, almost half of the Lease quartz plot towards the hydrothermal section of the ternary diagram (magmatic-hydrothermal quartz). The quartz from the Lease Granite becomes increasingly Ti-depleted and appreciably more Al- and Ge-rich than the Nebo and Bobbejaankop quartz (Fig. 9a). In contrast, the pipe quartz is notably Ti-poor and plots primarily along the base of the ternary diagram (hydrothermal quartz) (Fig. 9a). The Al/Ti and Ge/Ti ratios of the quartz show similar trends to the Ti-Ge-Al ternary diagram. A sequential increase in these ratios from the Nebo through the Bobbejaankop and Lease to the pipe quartz, together with a well-correlated array, compositional overlap, and a co-linear trend imply a fractionating system along a single liquid line of descent (Fig. 9b).

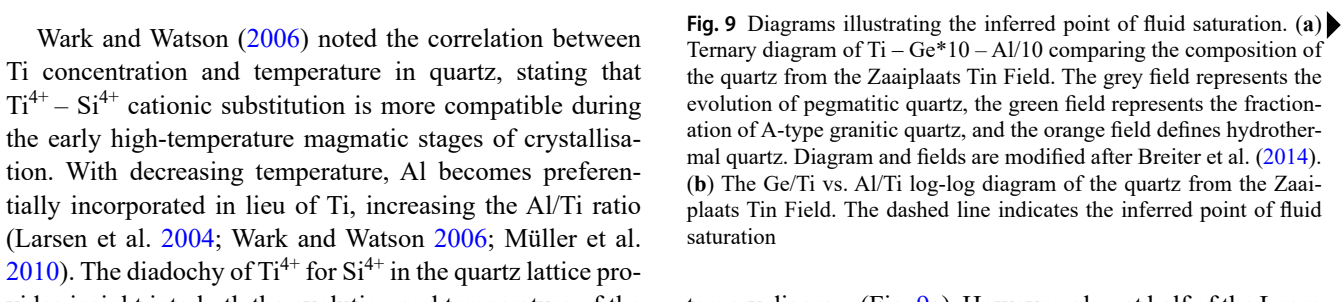

Fig. 9 Diagrams illustrating the inferred point of fluid saturation. (**a**) Ternary diagram of Ti – Ge*10 – Al/10 comparing the composition of the quartz from the Zaaiplaats Tin Field. The grey field represents the evolution of pegmatitic quartz, the green field represents the fractionation of A-type granitic quartz, and the orange field defines hydrothermal quartz. Diagram and fields are modified after Breiter et al. (2014). (**b**) The Ge/Ti vs. Al/Ti log-log diagram of the quartz from the Zaaiplaats Tin Field. The dashed line indicates the inferred point of fluid saturation

In addition to recording the evolution of the granites, there is a distinct gap along the compositional array of data, shown by both the Ti-Ge-Al and Ge/Ti vs. Al/Ti diagrams (Fig. 9). This compositional gap is interpreted to be the point of fluid saturation within these granites. The quartz compositions towards the Ti apex (Fig. 9a) with higher Ti, lower Ge/Ti and Al/Ti values represent the magmatic phase (Fig. 9). The compositional trend away from the Ti apex towards a more magmatic-hydrothermal regime is primarily controlled by feldspar fractionation. Beyond the compositional gap, the magmatic-hydrothermal quartz that formed in a fluid-saturated environment is more compositionally variable and increasingly Ti-deficient in some of the Bobbejaankop and most of the Lease quartz (Fig. 9). The hydrothermal pipe quartz on both diagrams plots at the end of the compositional arrays (lower Ti, higher Al/Ti and Ge/Ti), and is considered to represent late-stage magmatic-hydrothermal quartz. Therefore, the quartz trace element systematics are able to record fluid saturation and accumulation upwards in a granitic cupola, and reflect the magmatic to magmatic-hydrothermal transition in evolving granites (Fig. 9). This interpretation of the compositional evolution of the ZTF, recorded by quartz, corresponds with the model suggested by Vonopartis et al. (2020) and subsequent research (Gardiner et al. 2021; Vonopartis et al. 2022).

As an incompatible element, B^{3+} may also be incorporated into the quartz structure by coupled substitution (Larsen et al. 2004; Götze et al. 2021). Since tourmaline is a common accessory in the Bobbejaankop and Lease granites, B is a likely component in this system. The B content

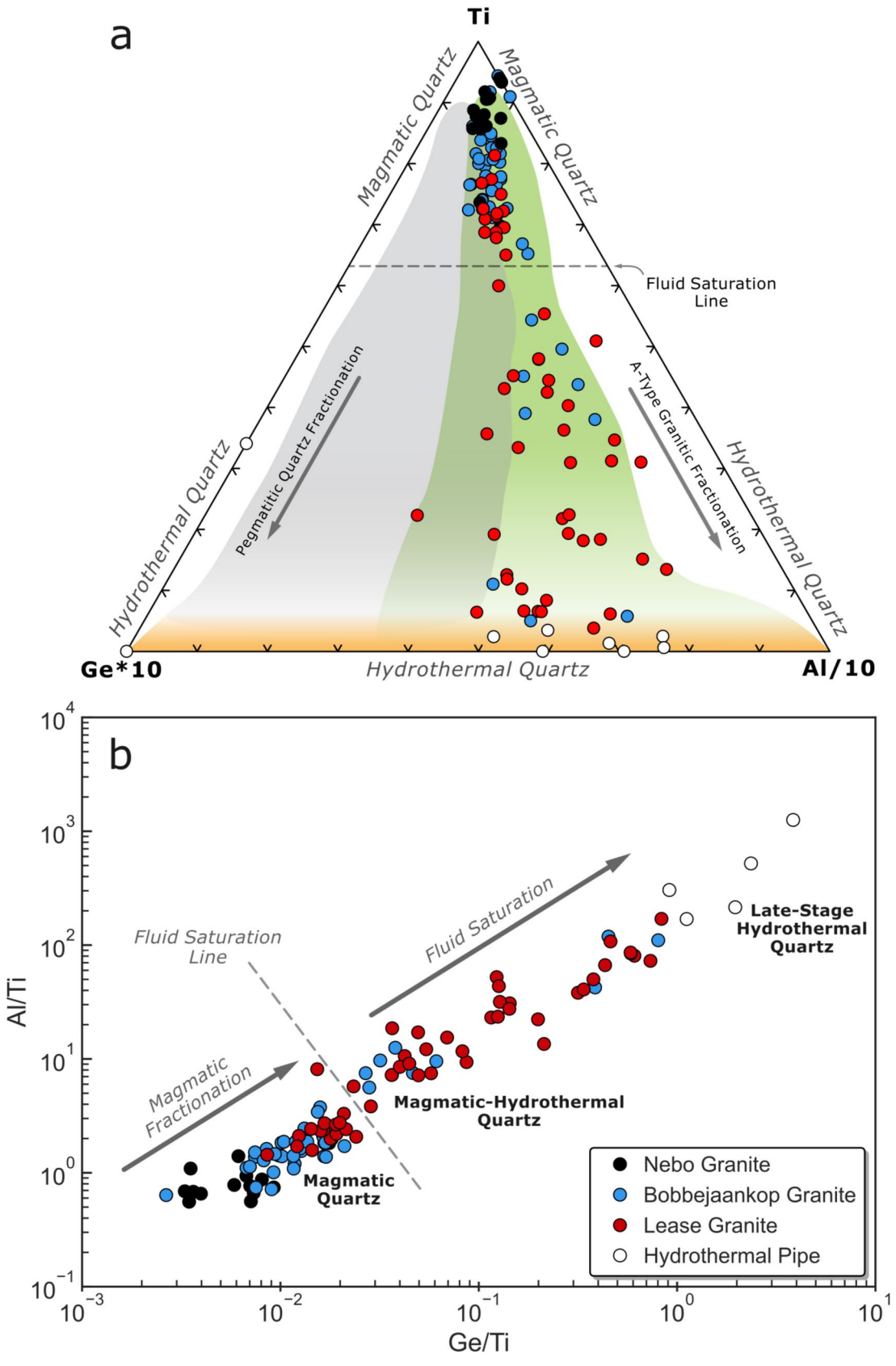
a
Ti
Magmatic Quartz
Magmatic Quartz
Fluid Saturation Line
Pegmatitic Quartz Fractionation
A-Type Granitic Fractionation
Hydrothermal Quartz
Hydrothermal Quartz
Hydrothermal Quartz
Ge*10
Al/10
b
Al/Ti
Ge/Ti
Fluid Saturation Line
Fluid Saturation
Magmatic Fractionation
Late-Stage Hydrothermal Quartz
Magmatic-Hydrothermal Quartz
Magmatic Quartz
Nebo Granite
Bobbejaankop Granite
Lease Granite
Hydrothermal Pipe

of the Nebo quartz is relatively low, between 0.45 and 4.1 ppm, and is comparable to quartz from tourmaline-free pegmatites (Breiter and Müller 2009; Götze et al. 2021). The average B content of the Bobbejaankop and Lease quartz is 3.3 and 6.2 ppm, however, they reach 34 and 49 ppm, respectively (Fig. 7). In general, the B content in quartz is commonly low, between <1 to 25 ppm, with up to 46 ppm recorded in quartz from agates (Müller et al. 2012; Götze et al. 2020, 2021). Therefore, it is possible that the variable B content of the Bobbejaankop and Lease quartz may be due to nano- and micro-inclusions of tourmaline (Müller et al. 2012; Götze et al. 2021). Despite the extensive tourmalinisation in the hydrothermal pipes, the B content from the pipe quartz is similar to the lower values in the Lease quartz.

As shown earlier, Ge, Al, Li, and Be substitute for Si^{4+} in quartz within lower-temperature, more evolved granitic systems, increasing from Nebo to Bobbejaankop then Lease to the pipe quartz (Fig. 7). These elements are not readily modified in quartz by sub-solidus processes (Larsen et al. 2004; Jacamon and Larsen 2009). The range of Ge in quartz from the ZTF is within the range of magmatic quartz (Jacamon and Larsen 2009; Müller et al. 2018), although this magmatic signature is also not uncommon in hydrothermal quartz (akin to the pipe quartz). Quartz from other fractionated and similarly tourmalinised granites, such as the Heemskirk granite in Tasmania (Hong et al. 2019), exhibit similar ranges in Ge content, in both magmatic and hydrothermal quartz populations. Therefore, the magmatic Ge signatures and linear correlation of quartz composition from the pipes and the granites, are consistent with their formation from internally-derived magmatic-hydrothermal fluids.

Beryllium exhibits an increase with fractionation in the quartz, similar to B and Li. However, the Be contents in quartz from the hydrothermal pipes do not follow the enrichment trend defined by the granites (Fig. 7). The noticeable Be-depletion in the quartz from the pipes may be attributed to the loss of Be during their formation. This resulted in the pipe quartz having a comparable Be content to the Lease quartz, despite their late-stage hydrothermal origin. Breiter and Müller (2009) describe the sequential enrichment of incompatible elements, such as Ge and Be, in the later-stages of A-Type granitic quartz from the Erzgebirge/Krušné Hory Mountains and highlight a loss of Be in the most evolved samples. The depletion of Be is ascribed to the partitioning of Be into a late-stage fluid phase and the formation of beryl-bearing fissures (Breiter and Müller 2009). A similar loss of Be from the pipes may be a plausible explanation, although this is inconclusive as there is no documented beryl from the ZTF.

Petrogenesis

The magmatic to magmatic-hydrothermal evolution exhibited by quartz compositional data along traverses can be distinguished into ten steps and four generalised stages of quartz formation (Fig. 10; Table 2). This interpretation and grouping of quartz compositional types are based on the abundance of structurally incorporated trace elements and CL characteristics that are observed between the various quartz populations (Fig. 10). The stages and compositional variations are summarised in Table 2.

The first stage in the evolution of the system is magmatic. It is represented by Nebo quartz and cores of the Bobbejaankop quartz (*steps* 1 to 3), both of which have nearly identical Al and Ti abundances, similar low Sn contents, as well as similar luminescence and textures (Fig. 10a; Table 2). The second stage is reflected by the rim compositions of the Bobbejaankop quartz and cores of the Lease quartz (*steps 4* and *5*). The transition from stage 1 to 2 is characterised by a more muted CL luminescence, a decrease in Ti, and an increase in Al content (Fig. 10a; Table 2). Therefore, it is likely that Stage 2 (*steps 4* and *5*) formed in

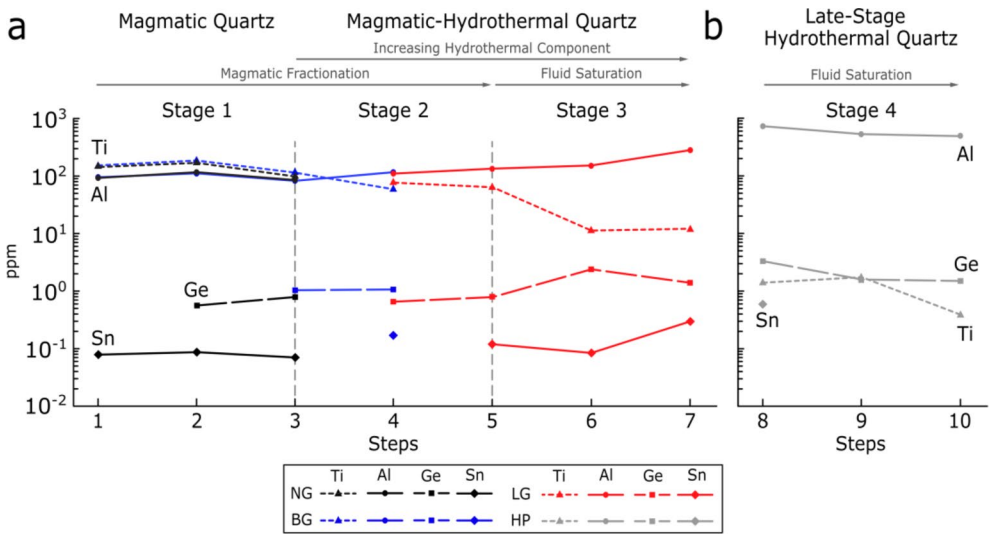

Fig. 10 Compilation of the quartz traverses shown in Fig. 8. The interpreted sequence of quartz compositions (steps) is ordered based on the abundances of Ti, Al, Ge, and Sn, with respect to the evolution of the Zaaiplaats Tin Field (Vonopartis et al. 2020). (**a**) The Nebo, Bobbejaankop, and Lease quartz represent the evolution of magmatic to magmatic-hydrothermal quartz. (**b**) The Tourmaline-Quartz Pipe represents a distinct late-stage hydrothermal quartz population. Abbreviations: Nebo Granite (NG); Bobbejaankop Granite (BG); Lease Granite (LG); and hydrothermal pipe (HP)

Table 2 Stages of quartz formation and their trace element characteristics from the ZTF

Stage.	Lithology	Trace Elements	Petrogenetic Insight
Magmatic Quartz			
1	Nebo Quartz Bobbejaankop Quartz (Core)	− Al < Ti − Low Ge − Low Sn*	Formation within a granitic magma
Early Magmatic-Hydrothermal Quartz			
2	Bobbejaankop Quartz (Rim) Early-Lease Quartz (Core)	− Al > Ti − Moderate Ge − Moderate Sn*	The magmatic-hydrothermal fluid component in crystallising magma
Fluid Saturation – Magmatic-Hydrothermal Transition			
3	Lease Quartz (Rim)	− High Al − Low Ti − Moderate Ge − Moderate to high Sn*	Saturation of a magmatic-hydrothermal fluid in the granite cupola
Late-Stage Hydrothermal Fluid			
4	Hydrothermal Pipe	− Very High Al − Very Low Ti − Moderate Ge − High Sn*	Formation from an acidic, metal-bearing magmatic-hydrothermal fluid

*Non-structural element in quartz

a slightly lower temperature environment, which is consistent with the Ti depletion in the margin of the Bobbejaankop quartz and cores of the Lease quartz (e.g. Wark and Watson 2006; Breiter and Müller 2009).

The Sn content in the Nebo Granite remains constant, whereas Sn contents are low and only measurable in the final generation of the Bobbejaankop quartz (*Stage 2*) (Fig. 10a; Table 2). The variations in Sn content are attributed to its distribution in the various host lithologies. As there is no cassiterite mineralisation in the Nebo Granite, Sn is likely hosted in cassiterite or within saline fluids trapped in inclusions. The early Bobbejaankop quartz is considered to be magmatic (*Stage 1*), similar to the Nebo Granite quartz. The subsequent introduction of Sn, by Sn-bearing hydrothermal fluids, and possible liberation of Sn from minerals such as biotite, during alteration, is recorded by the Bobbejaankop quartz rims (*Stage 2*) (Fig. 10a; Table 2). The interior of the Lease quartz has similar Al and Ti content, and a similar Sn-concentrations to the Bobbejaankop quartz rim (*steps 4* and *5*). Thus, it is reasonable to suggest that the initial Lease quartz crystallised from an environment, similar in composition to the final stages of Bobbejaankop Granite (*Stage 2*).

The third stage shows a distinct compositional shift that is considered to reflect the point of fluid-saturation during the final formation of the Lease Granite (*Stage 3*). *Stage 3* is characterised by a sharp Ti depletion and simultaneous Al and Ge enrichment towards the rims of the Lease quartz (*steps 6* and *7*) (Fig. 10a; Table 2). This is concomitant with a lowered granitic solidus, that reduced the incorporation of Ti into the quartz lattice.

An increase in acidity is consistent with the documented increase of late-stage greisenisation in the Lease Granite. This would have enhanced the dissolution of feldspar, chlorite, and mica, resulting in the liberation of Al, Ti, and possibly Sn (Zhao et al. 2005; Vonopartis et al. 2020). As Ti has been documented to affect the CL response of quartz (Müller et al. 2003), the liberation of Ti into the fluid during chloritisation and greisenisation of proximal mica and chlorite in miarolitic cavities, may explain the thin, strongly luminescent rims on the miarolitic quartz.

The fourth and final stage comprises the quartz from the hydrothermal pipes. This late quartz is characterised by the lowest Ti and the highest Al and Ge contents in the quartz populations (*steps 8* to *10*) (Fig. 10b; Table 2). The high Ge and very high Al content is characteristic of quartz that crystallised from a highly fractionated, hydrothermal fluid (Müller et al. 2018) with a significantly lower crystallisation temperature than that of the granitic quartz, as reflected in the low Ti content. The hydrothermal pipes are host to the highest Sn grades in the ZTF (Crocker et al. 2001; Vonopartis et al. 2020), therefore a high quartz Sn content in quartz might be expected. However, the pipe quartz is generally Sn poor, despite the single highest Sn-in-quartz content measured from the core of one pipe quartz (Fig. 10b). Thus, the pipe quartz is distinct in the evolution of the ZTF (*Stage 4*) and is corroborated by the petrological evidence of extensive greisenisation (Strauss 1954; Pollard et al. 1989; Crocker et al. 2001; Vonopartis et al. 2020) and low temperature α-quartz observed within the hydrothermal pipes (Fig. 6b, c).

Insight into Sn-mineralisation

Tin is considered an incompatible and fluid mobile element, depending on its oxidation state, allowing it to be readily concentrated via granitic fractionation and hydrothermal mobilisation (Wolf et al. 2018; Lehmann 2020; Vasyukova and Williams-Jones 2020). The Lease Granite is the most fractionated, hydrothermally altered, and mineralised of the three granitic lithologies. These characteristics are identified geochemically by the Al/Ti and Ge/Ti ratios in quartz (Fig. 9b) and supported by whole-rock trace elemental ratios such as Rb/Sr and Zr/Hf (Vonopartis et al. 2020, 2021). Most of the quartz from the Lease Granite is inferred to have formed after fluid saturation suggesting that the Sn content should be higher than that derived from fractionation alone.

The average Sn-in-quartz content from the Nebo Granite (0.17 ppm) is close to the estimated Sn content of the Primitive Mantle of ± 0.14 ppm (Palme et al. 2003) and reaches 21 ppm within the Lease quartz. However, the Sn abundances across all the quartz stages generally range from below detection to 2.3 ppm, comparable to quartz from other

mineralised granitoids and pegmatites (Götze et al. 2004; Breiter et al. 2014; Hong et al. 2019). The Sn-in-quartz content of the hydrothermal pipes is typically below detection and therefore the Sn content of the pipe quartz is inconclusive. Tin is not easily incorporated into the quartz lattice and thus Sn-in-quartz may be considered an indication of the Sn content of the magmatic-hydrothermal environment. Thus, a late-stage depletion of Sn-in-quartz from fractionated lithologies that is not reflected in the whole-rock Sn content, would perhaps indicate the precipitation of cassiterite. The relationship between the whole-rock Sn and Sn-in-quartz content, together with the identification of lithologies formed after the point of fluid-saturation, shows promise to be used as a vector to endogranitic Sn-mineralisation.

Conclusion

The textural and trace element investigations of quartz from the ZTF provides insight into the magmatic-hydrothermal evolution of stanniferous Bushveld Granites. The evolution of the Nebo to Lease Granite is typical of an evolving A-Type granite system that transitions from a magmatic to magmatic-hydrothermal regime, and ultimately to a late-stage hydrothermal phase. The CL textures and the Al/Ti and Ge/Ti ratios of the Nebo quartz and early generations of the Bobbejaankop quartz indicate a magmatic origin. The later generations of the Bobbejaankop quartz, however, exhibit a decrease in Ti and an increase in Al and Ge, indicating an increasing magmatic-hydrothermal influence. These increasingly hydrothermal characteristics continued into the Lease quartz and mark the onset of fluid saturation in the system.

Thus, the petrographic and geochemical evolution of quartz points to a fractionating granitic system that became increasingly fluid-saturated towards the apical portions of the intrusion. The late-stage pipe quartz exhibits distinctly hydrothermal textures, CL features, is Ti depleted, and exhibits notably high Al and Ge contents. These are characteristics of a late-stage, hydrothermal fluid, which likely exsolved from the Bobbejaankop and Lease Granites. Therefore, trace element contents in quartz demonstrate the ability to record the magmatic to magmatic-hydrothermal transition and potentially identify the onset of fluid-saturation in a granitic system.

In addition, there is an observable increase in Sn content of quartz with a correlated increase in the Sn content of the hosting granite. However, the Sn content of the quartz from the highly mineralised hydrothermal pipes is below detection. This late-stage depletion of Sn-in-quartz is not observed in the whole-rock composition and indicates the concomitant crystallisation of cassiterite. The decoupling of Sn-in-quartz and whole rock Sn content, together with a recognition of the onset of fluid saturation, is therefore proposed as a potential vector towards endogranitic Sn mineralisation. The insight gained from trace element analysis of quartz and its use as a vector is likely not restricted to granite-related mineralisation and can be used for the exploration for other hydrothermal deposits.

Supplementary Information The online version contains supplementary material available at https://doi.org/10.1007/s00126-025-01363-x.

Acknowledgements We would like to thank VM Investment Co. and Andrada Mining for support and access to the Zaaiplaats Tin Field. We further thank Editor-in-Chief Bernd Lehmann, Assistant Editor Frank Melcher, and reviewer Simon Goldmann for their detailed review and valuable contributions to the improvement of this manuscript.

Author contributions L. C. Vonopartis – writing, conceptualising, editing, analysis, and data handling; P. A. M. Nex, J. A. Kinnaird, and L. J. Robb – writing and editing; and R. Bolhar – data reduction, analysis, and editing. All authors have read and agree to the published version of the manuscript.

Funding Open access funding provided by University of the Witwatersrand.
This research was funded by the THRIP (Technology and Human Resources for Industry Programme). JK and PN acknowledge financial support for research from CIMERA. RB acknowledges funding through a NRF-NEP grant (UID-105674) to establish the LA-SF-ICP-MS and quadrupole ICP-MS facility at the University of the Witwatersrand.

Data availability The data of this study are available online with this manuscript as supplementary files.

Declarations

Competing interest The authors declare that there are no financial or non-financial interests that have influenced this research.

References

Audétat A, Garbe-Schönberg D, Kronz A et al (2015) Characterisation of a natural quartz crystal as a reference material for

microanalytical determination of Ti, al, Li, Fe, Mn, Ga and ge. Geostand Geoanalytical Res 39:171–184
Bailie RH, Robb LJ (2004) Polymetallic mineralization in the granites of the Bushveld Complex - examples from the central southeastern lobe. South Afr J Geol 107:633–652
Breiter K, Müller A (2009) Evolution of rare metal-specialised granite melt documented by quartz chemistry. Eur J Mineral 21:335–346. https://doi.org/10.1127/0935-1221/2009/0021-1907
Breiter K, Ackerman L, Ďurišová J et al (2014) Trace element composition of quartz from different types of pegmatites: A case study from the Moldanubian zone of the Bohemian Massif (Czech Republic). Mineral Mag 78:703–722
Breiter K, Ďurišová J, Dosbaba M (2020) Chemical signature of quartz from S- and A-type rare-metal granites– a summary. Ore Geol Rev 125:103674. https://doi.org/10.1016/j.oregeorev.2020.103674
Coetzee J (1984) A geochemical and petrographical investigation of the low-grade Tin deposits in the Bobbejaankop granite at the Zaaiplaats Tin mine. Unpub MSc Univ Pretoria Unpub. M.Sc:126
Crocker IT, Eales HV, Ehlers DL (2001) The fluorite, cassiterite and sulphide deposits associated with the acid rocks of the Bushveld Complex. Council for Geoscience
Cui X, Wang Q, Deng J et al (2019) Genesis of the Xiaolonghe quartz vein type Sn deposit, SW China: insights from cathodoluminescence textures and trace elements of quartz, fluid inclusions, and oxygen isotopes. Ore Geol Rev 111:102929
Dyck B (2023) Sticking together: mechanisms of quartz synneusis in high-silica magma. Geosci Front 14:101512. https://doi.org/10.1016/j.gsf.2022.101512
Finn CA, Bedrosian PA, Cole JC et al (2015) Mapping the 3D extent of the Northern lobe of the Bushveld layered mafic intrusion from geophysical data. Precambrian Res 268:279–294
Gao S, Liu X, Yuan H et al (2002) Determination of Forty two major and trace elements in USGS and NIST SRM glasses by laser ablation-inductively coupled plasma-mass spectrometry. Geostand Newsl 26:181–196
Gardiner NJ, Hawkesworth CJ, Robb LJ et al (2021) Metal anomalies in Zircon as a record of granite-hosted mineralization. Chem Geol 585:120580. https://doi.org/10.1016/j.chemgeo.2021.120580
Götze J (2009) Chemistry, textures and physical properties of quartz—geological interpretation and technical application. Mineral Mag 73:645–671
Götze J, Möckel R (eds) (2012) Quartz: deposits, mineralogy and analytics. Springer, Berlin
Götze J, Plötze M, Graupner T et al (2004) Trace element incorporation into quartz: a combined study by ICP-MS, electron spin resonance, cathodoluminescence, capillary ion analysis, and gas chromatography. Geochim Cosmochim Acta 68:3741–3759
Götze J, Möckel R, Pan Y (2020) Mineralogy, geochemistry and genesis of Agate—A. Rev Minerals 10:1037. https://doi.org/10.3390/min10111037
Götze J, Pan Y, Müller A (2021) Mineralogy and mineral chemistry of quartz: A review. Mineral Mag 85:639–664. https://doi.org/10.1180/mgm.2021.72
Hallbauer DK (1992) The use of selected trace elements in vein quartz and quartz pebbles in identifying processes of formation and source rocks. Geol Soc South Afr 24:157–159
Heaney PJ, Prewitt CT, Gibbs GV (2018) Silica: physical behavior, geochemistry, and materials applications. Walter de Gruyter GmbH & Co KG
Hill M, Barker F, Hunter D, Knight R (1996) Geochemical characteristics and origin of the Lebowa granite suite, Bushveld Complex. Int Geol Rev 38:195–227
Hong W, Cooke DR, Zhang L et al (2019) Cathodoluminescence features, trace elements, and oxygen isotopes of quartz in unidirectional solidification textures from the Sn-mineralized Heemskirk granite, Western Tasmania. Am Mineral 104:100–117
Howie RA, Zussman J, Deer W (1992) An introduction to the rock-forming minerals, 2nd edn. Longman, New York
Hu Z, Gao S, Liu Y, Hu S, Chen H, Yuan H (2008) Signal enhancement in laser ablation ICP-MS by addition of nitrogen in the central channel gas. J Anal Spectrom 23:1093–1101
Huang R, Audétat A (2012) The titanium-in-quartz (TitaniQ) thermobarometer: A critical examination and re-calibration. Geochim Cosmochim Acta 84:75–89
Hunter DR (1975) The regional geological setting of the Bushveld Complex (An adjunct to the provisional tectonic map of the bushveld complex). Univ Witwatersrand Econ Geol Res Unit, p 18
Jacamon F, Larsen RB (2009) Trace element evolution of quartz in the Charnockitic Kleivan granite, SW-Norway: the Ge/Ti ratio of quartz as an index of igneous differentiation. Lithos 107:281–291
Jochum KP, Weis U, Stoll B et al (2011) Determination of reference values for NIST SRM 610–617 glasses following ISO guidelines. Geostand Geoanalytical Res 35:397–429
Keyser W, Müller A, Knoll T et al (2023) Quartz chemistry of lithium pegmatites and its petrogenetic and economic implications: examples from Wolfsberg (Austria) and Moylisha (Ireland). Chem Geol 630:121507. https://doi.org/10.1016/j.chemgeo.2023.121507
Kinnaird JA, Kruger FJ, Cawthorn RG (2004) Rb-Sr and Nd-Sm isotopes in fluorite related to the granites of the Bushveld Complex. South Afr J Geol 107:413–430
Larsen RB, Henderson I, Ihlen PM, Jacamon F (2004) Distribution and petrogenetic behaviour of trace elements in granitic pegmatite quartz from South Norway. Contrib Mineral Petrol 147:615–628
Larsen RB, Jacamon F, Kronz A (2009) Trace element chemistry and textures of quartz during the magmatic hydrothermal transition of Oslo rift granites. Mineral Mag 73:691–707
Lehmann B (2020) Formation of tin ore deposits: a reassessment. Lithos 105756:402–403
Monecke T, Kempe U, Petersen S et al (1999) Trace element characteristics of quartz from the TAG hydrothermal mound (Mid-Atlantic ridge at 26 08′ N). Min Depos Process Process Balkema Rotterdam Neth 551:554
Monecke T, Kempe U, Monecke J et al (2002) Tetrad effect in rare Earth element distribution patterns: a method of quantification with application to rock and mineral samples from granite-related rare metal deposits. Geochim Cosmochim Acta 66:1185–1196
Müller A, Koch-Müller M (2009) Hydrogen speciation and trace element contents of igneous, hydrothermal and metamorphic quartz from Norway. Mineral Mag 73:569–583
Müller A, Seltmann R, Behr H-J (2000) Application of cathodoluminescence to magmatic quartz in a Tin granite–case study from the Schellerhau granite complex, Eastern Erzgebirge, Germany. Miner Deposita 35:169–189
Müller A, René M, Behr H-J, Kronz A (2003) Trace elements and cathodoluminescence of igneous quartz in Topaz granites from the hub stock (Slavkovský les Mts., Czech Republic). Mineral Petrol 79:167–191
Müller A, Ihlen PM, Kronz A (2008) Quartz chemistry in polygeneration Sveconorwegian pegmatites, Froland, Norway. Eur J Mineral 20:447–463
Müller A, Kerkhof AM, van den, Behr H-J et al (2010) The evolution of late-Hercynian granites and rhyolites documented by quartz—a review. Earth Environ Sci Trans R Soc Edinb 100:185–204
Müller A, Wanvik JE, Ihlen PM (2012) Petrological and chemical characterisation of high-purity quartz deposits with examples from Norway. In: Götze J, Möckel R (eds) Quartz: deposits, mineralogy and analytics. Springer, Berlin, Heidelberg, pp 71–118

Müller A, Herklotz G, Giegling H (2018) Chemistry of quartz related to the Zinnwald/Cínovec Sn-W-Li greisen-type deposit, Eastern Erzgebirge, Germany. J Geochem Explor 190:357–373

Müller A, Keyser W, Simmons WB et al (2021) Quartz chemistry of granitic pegmatites: implications for classification, genesis and exploration. Chem Geol 584:120507. https://doi.org/10.1016/j.chemgeo.2021.120507

Nesse WD (2009) Introduction to mineralogy. Oxford University Press, New York

Palme H, O'Neill HSC, Carlson RW (2003) Cosmochemical estimates of mantle composition. The mantle and core. In: Holland HD, Turekian KK (eds) Treatise on geochemistry, 2nd edn. Elsevier, pp 1–35

Paton C, Woodhead JD, Hellstrom JC et al (2010) Improved laser ablation U-Pb Zircon geochronology through robust downhole fractionation correction. Geochem Geophys Geosyst 11:1–36

Paton C, Hellstrom J, Paul B et al (2011) Iolite: freeware for the visualisation and processing of mass spectrometric data. J Anal Spectrom 26:2508–2518

Pollard PJ, Taylor RG, Tate NM (1989) Textural evidence for quartz and feldspar dissolution as a mechanism of formation for Maggs pipe, Zaaiplaats Tin mine, South Africa. Miner Deposita 24:210–218

Pollard PJ, Andrew AS, Taylor RG (1991) Fluid inclusion and stable isotope evidence for interaction between granites and magmatic hydrothermal fluids during formation of disseminated and Pipe-Style mineralization at the Zaaiplaats Tin mine. Econ Geol 86:121–141

Robb LJ, Freeman LA, Armstrong RA (2000) Nature and longevity of hydrothermal fluid flow and mineralisation in granites of the Bushveld Complex, South Africa. Earth Environ Sci Trans R Soc Edinb 91:269–281

Rusk B, Reed M (2002) Scanning electron microscope–cathodoluminescence analysis of quartz reveals complex growth histories in veins from the Butte porphyry copper deposit. Mont Geol 30:727–730

SACS (1980) Stratigraphy of South Africa. Part 1 (L.E. Kent, comp.), lithostratigraphy of the Republic of South Africa. Handb Geol Surv South Afr 8:690

Schrön W, Schmädicke E, Thomas R, Schmidt W (1988) Geochemische untersuchungen an pegmatitquarzen. Z Für Geol Wiss 16:229–244

Scoates JS, Wall CJ, Friedman RM et al (2021) Dating the Bushveld Complex: timing of crystallization, duration of magmatism, and cooling of the world's largest layered intrusion and related rocks. J Petrol 62:egaa107

Skursch O, Tegner C, Lesher CE, Cawthorn RG (2020) Two expressions of the transition from mafic cumulates to granitoids in the bushveld complex, South Africa: examples from the Western and Eastern limbs. Lithos 105671:372–373

Strauss CA (1954) The geology and mineral deposits of the potgietersrus tinfields. South Afr Geol Surv Mem 46:241

Suttner LJ, Leininger RK (1972) Comparison of the trace element content of plutonic, volcanic, and metamorphic quartz from Southwestern Montana. Geol Soc Am Bull 83:1855–1862

Uysal IT, Gasparon M, Bolhar R et al (2011) Trace element composition of near-surface silica deposits—A powerful tool for detecting hydrothermal mineral and energy resources. Chem Geol 280:154–169. https://doi.org/10.1016/j.chemgeo.2010.11.005

Vasyukova O, Williams-Jones A (2020) Partial melting, fractional crystallisation, liquid immiscibility and hydrothermal mobilisation–A 'recipe' for the formation of economic A-type granite-hosted HFSE deposits. Lithos 356:105300

Vonopartis LC, Nex PAM, Kinnaird JK, Robb LJ (2020) Evaluating the changes from endogranitic magmatic to magmatic-hydrothermal mineralization: the Zaaiplaats Tin granites, Bushveld igneous complex, South Africa. Minerals 10. https://doi.org/10.3390/min10040379

Vonopartis LC, Kinnaird JA, Nex PAM, Robb LJ (2021) African A-Type granites: a geochemical review on metallogenic potential. Lithos 396–397. https://doi.org/10.1016/j.lithos.2021.106229

Vonopartis LC, Booysen R, Nex PAM et al (2022) Combined satellite and portable XRF exploration mapping of the Zaaiplaats Tin field, South Africa. South Afr J Geol 125:45–60. https://doi.org/10.25131/sajg.125.0006

Wark DA, Watson EB (2006) TitaniQ: a titanium-in-quartz geothermometer. Contrib Mineral Petrol 152:743–754

Webb SJ, Ashwal LD, Cawthorn RG (2011) Continuity between Eastern and Western Bushveld Complex, South Africa, confirmed by xenoliths from kimberlite. Contrib Mineral Petrol 162:101–107. https://doi.org/10.1007/s00410-010-0586-z

Wilson MGC, Anhaeusser CR (1998) The mineral resources of South Africa, 6th edn. Council for Geosciences

Wolf M, Romer RL, Franz L, López-Moro FJ (2018) Tin in granitic melts: the role of melting temperature and protolith composition. Lithos 310:20–30

Zeh A, Ovtcharova M, Wilson AH, Schaltegger U (2015) The Bushveld Complex was emplaced and cooled in less than one million years– results of zirconology, and geotectonic implications. Earth Planet Sci Lett 418:103–114

Zhao K-D, Jiang S-Y, Jiang Y-H, Wang R-C (2005) Mineral chemistry of the Qitianling granitoid and the furong Tin ore deposit in Hunan Province, South China: implication for the genesis of granite and related Tin mineralization. Eur J Mineral 17:635–648